A hadronic synchrotron mirror model for blazar - Application to 3C279

LL Oberholzer

orcid.org 0000-0003-2686-1266

Dissertation accepted in partial fulfilment of the requirements for the degree *Master of Science in Astrophysical Sciences* at the North-West University

Supervisor: Prof M Boettcher

Graduation December 2021

24933627

Acknowledgements

A big thank you to NASSP, the NRF, the Centre for Space Research, and my Professor, Markus Böttcher; without whom this dissertation would not be possible financially. Professor Böttcher, I can't thank you enough for the support, patience and kindness you showed me throughout the whole project, I really admire you and I learned a lot. All the scientists and staff at the Centre for Space Research, thank you for everyone who has made a small contribution to my project, a little bit of advice on time management, or even sitting next to me and helping me to debug my programming. I want to thank every single person who prayed for me and supported me through this process. My friends that would not allow me to fall into negativity, Lize, Sarah, Elishia and Anri. My wonderful Boyfriend Ruan, who had to sit through all the different stages of frustration and breakthrough, thank you for being supportive. My parents for caring so much and understanding when I can't come home as often, as well as my other family members that supported me through this, Sarah, my sisters, Heike and Inge, and Raphael my brother. I am extremely grateful to God for giving me the strength to carry on and never consider giving up, for giving me every skill I was able to use and teaching me valuable lessons along the way and planting me in a church, Unite180, where everyone was also rooting for me in this matter.

Abstract

Blazars are a class of Active Galactic Nuclei (AGN) that are radio loud and have a small angle between the jet and the observer's line of sight, found in the centres of elliptical galaxies. In some cases, flaring events in one frequency band are not accompanied by flaring in other bands, termed - orphan flares. The causes of this variability and conditions in and location of the high energy emission region are not completely understood. As a possible explanation for rapid gamma-ray variability, the hadronic mirror model is suggested. A TeV orphan flare was observed on the 28th of January 2018 by the H.E.S.S. observatoty from 3C 279. A primary flare was observed 11 days earlier by Fermi-LAT. A broken power-law is applied to the Fermi-LAT spectrum preceding the orphan flare to constrain model parameters able to reproduce the proton-synchrotron SED through an analytical fit to the data. The high-energy component of the flare is modeled by the hadronic synchrotron mirror model. The model predicted a dense enough target photon field that is sufficiently efficient for photohadronic interactions to take place and the Fermi flux was not lifted a lot by this model unlike the VHE flux. The photo-pion component of the spectrum is comparable in flux to that of the proton-synchrotron component.

Keywords - AGN, blazar, hadronic model, relativistic astrophysics

Contents

List of Figures

List of Tables

Chapter 1

Background

1.1 Introduction

In a galaxy far far away, called 3C 279, there is an active galactic nucleus (AGN) with some very variable mood swings, let us tell its story...

Blazars are a subclass of active galactic nuclei that are radio loud and found in the centres of elliptical galaxies. There are two types, flat spectrum radio quasars (FSRQs), if they have strong emission lines, like 3C 279, and BL Lac objects if they have weak emission lines [Böttcher, 2007]. Most blazars are γ-ray loud due to relativistic jets pointed at a small angle with respect to our line of sight. Due to this geometry, their emission is Doppler boosted, and the jets have been seen through radio interferometry to exhibit apparent superluminal motion [Zensus and Porcas, 1986]. The spectral energy distributions (SEDs) of blazars are characterized by two humps or components. The first hump is the low-frequency component that is caused by electron synchrotron emission. For the second hump, the high-frequency component in leptonic models is caused by Compton scattering [Maraschi et al., 1992, Dermer and Schlickeiser, 1993, Bloom and Marscher, 1996]. However, alternatively this component can also be caused by hadronic processes [Mücke et al., 2003, Mannheim and Biermann, 1992, Aharonian, 2000], where the dominant gamma-ray emission mechanisms are proton-synchrotron radiation and synchrotron emission from secondary particles produced by photo-pion production. These reactions are displayed by the following:

$$p + \gamma \rightarrow p + \pi^0 \rightarrow p + \gamma + \gamma \tag{1.1}$$

$$\text{or } \rightarrow n + \pi^+ \rightarrow n + \mu^+ + \nu_\mu \rightarrow n + e^+ + \nu_\mu + \nu_e + \bar{\nu_\mu} \tag{1.2}$$

Blazars show extreme variability across the electromagnetic spectrum. The central engines causing the relativistic jets have quiescent states and flaring states. Some of these flares are characterised by extremely fast variability of timescales

down to a few minutes. Examples of blazars beside 3C 279 that showcase these minute-scale variabilities are Mrk 501, Mrk421 and PKS 2155-304, [Begelman et al., 2008, Konopelko et al., 2003, Aharonian et al., 2007, Sambruna et al., 2000]. In some cases, flaring events in one frequency band are not accompanied by flaring in other bands. Such events are termed orphan flares. Orphan flares are usually secondary flares following primary multi-wavelength flares, and are characterized by extreme variability [Krawczynski et al., 2004]. In this thesis we are specifically looking at an orphan TeV flare in the very-high-energy gamma-ray band ($E > 100\ GeV$). The causes of this variability and conditions in and location of the high energy emission region are not completely understood. Research on TeV blazars shows that leptonic jet models succesfully reproduce the SED through synchrotron self-Compton (SSC) radiation, where the second hump (or high-energy radiation) is produced by inverse Compton scattering of the electron-synchrotron radiation, [Pian et al., 1998, Kino et al., 2002]. The SSC model is not naturally able to reproduce orphan high-energy flares. When evaluating TeV orphan flares, it predicts quasi-simultaneous flaring in other wavebands like X-ray and optical bands. Considering an alternative to use a hadronic model would have important implications for the jet composition and energetics. Sikora and Madejski [2000] investigate the composition of jets, but the presence of protons does not make a hadronic model feasible, there needs to be enough power in the jet to accelerate these particles to relativistic energies. Hadrons require great amounts of power to be accelerated and thus require higher magnetic fields than leptonic models, but this also means that the proton processes will be carried out to larger distances on kiloparsec scale, because more enrgetic particles are accelerated, secondary interactions also produce high energy particles that escape absorption, which is consistent with TeV emission reaching the observer here on Earth, [Böttcher, 2005]. Photo-pion production can only happen if the protons have a dense target photon field to interact with. Such target photon fields can either be the co-spatially produced electron-synchrotron radiation, or radiation fields from outside the jet [Mannheim, 1993, Mannheim and Biermann, 1992]. Some more recent papers also conclude that there should be an external field (to create a dense target photon field) for the protons to interact with so that secondary interactions can produce these very high energy photons [Petropoulou et al., 2019] and [Aab et al., 2020]. Reimer et al. [2019] investigates the recent case of TXS 0506+056 with tentative neutrino associations and conclude that this case also requires an external field. The synchrotron mirror model proposed in this dissertation provides one possibility for such a target photon field. In this text, physical quantities will be parameterized by $Q = 10^x Q_x$ in c.g.s. units. Some of the cosmological parameters used throughout this study are the luminosity distance $d_L = 9.7 \times 10^{27}\ cm^2$ calculated as such from the redshift of 3C 279, $z = 0.536$.

1.1.1 Outline

Chapter 1 is an overview of the basic background on superluminal motion, AGN and the telescopes providing the observational data that are being interpreted in this thesis. Chapter 2 gives an overview on some blazar characteristics

and the object of this study, 3C 279. Chapter 3 gives some theoretical background on radiation mechanisms and leptonic and hadronic models. Chapter 4 describes the analytical part of the model used in this study in detail. Chapter 5 describes the numerical side of the modeling done in this dissertation and leads into Chapter 6 giving the results of the actual modeling. Chapter 7 concludes this dissertation.

1.2 Aim

The main motivation behind this study is to investigate what mechanisms produce orphan TeV flares. This research will help to investigate whether protons are accelerated to ultra-relativistic energies in the jets of blazars, which would be expected to be associated with the production of very-high-energy neutrinos. The variability of 3C 279 is sometimes correlated across the electromagnetic spectrum and sometimes not, as seen in other blazars as well, the results of this study might give a better perspective on why.

1.3 Active galactic nuclei

1.3.1 Structure of AGN

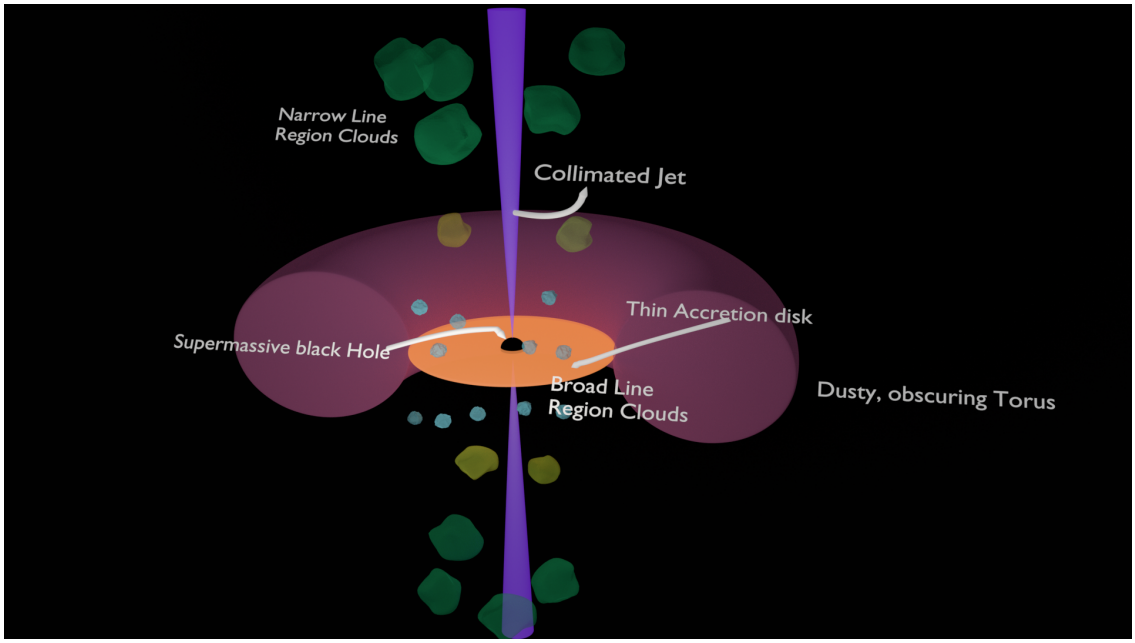

Figure 1.1: The structure of the AGN. Produced by Ruan de Jonge, an engineering student at the NWU, on Blender.

Active galactic nuclei are some of the most powerful and violent objects in the universe. Their structure, as shown in Figure 1.1, revolves around the central

engine, the supermassive black hole (SMBH). The black hole (BH) functions as a large gravitational potential well and accretes matter onto it, creating an accretion disk. This accretion disk is very luminous and reduces the angular momentum of matter pulled toward the black hole through turbulent and viscous processes [Urry and Padovani, 1995]. There are clouds of gas moving in the gravitational potential of the black hole that produce strong optical and ultraviolet emission lines. This region is called the broad line region (BLR) and the clouds are called broad line region clouds. These emission lines are obscured from certain lines of sight by a dusty torus [Urry and Padovani, 1995]. Much further from the central engine, narrow lines are produced by clouds, called narrow line region (NLR) clouds. Relativistic outflows of energetic particles sometimes occur along the rotation axis of the accretion disk, in about 10% of all AGN. The next sections will provide a brief overview of characteristic AGN features, keeping in mind that each feature is more complex than stated in this dissertation.

1.3.2 Accretion disk

The accretion disk forms a part of the central engine, a gaseous disk through which matter accretes onto the black hole (BH). Accretion disks are usually gas-pressure dominated [Urry and Padovani, 1995], when it becomes radiation-pressure dominated the accretion disk can feed into the BLR region [Bianchi et al., 2012]. The most natural assumption to make is that the accretion disk, dusty torus and black hole rotation share the same rotation axis due to the angular momentum conservation argument. It is possible, however, that if the black hole grows by unrelated accretion events then the BH's spin might be different to the rotation axis of the accretion disk [Bianchi et al., 2012].

1.3.3 Dusty torus

When looking at the accretion disk, it seems to be obscured by a parsec sized toroidal dust structure, hidden behind the dust of the Torus is the broad line region (BLR) [Jaffe et al., 2004]. The BLR and narrow line region (NLR) clouds (explained in the next subsection), are illuminated by the accretion disk. Scattering at right angles towards the observer induces polarization. Scattering takes place in the BLR and NLR regions. Looking at measured polarization angles and the fact that reflected broad lines are polarized, we see the need for an axisymmetric, toroidal absorber. In the case that the angles are different than measured and if the reflected broad lines were not polarised, then a different geometry than a toroidal shape would be warranted. If the symmetry of the polarization angles should be broken then the absorber should obstruct the nuclear radiation to be scattered in a specific range of angles. This specific range is obscured most naturally by a torus-shaped dust structure [Bianchi et al., 2012]. Studying the visibility of the BLR and the NLR, the torus size is constrained. The torus cannot be so great in size that it obscures the NLR, with typical sizes of 10-100 parsec, but needs to obscure the BLR, typical size below a parsec [Bianchi et al., 2012].

1.3.4 Broad line region

The BLR is formed by interstellar material that is being gravitationally pulled by the SMBH into the nucleus of the AGN structure. First this material forms the dusty torus, with a flattened distribution after losing angular momentum. Then the material moves into the dust sublimation radius and the dust evaporates to form the BLR. The BLR is dotted with clumps of clouds. These clouds are highly ionised on the front and are lowly ionised or neutral on the back [Gaskell, 2009]. BLR clouds are moving with a Keplerian velocity along the line of sight of the observer and therefore broad emission lines are often seen in the optical or UV range [Bianchi et al., 2012]. Hartman et al. [2001] writes that the BLR region of 3C 279 lies between $0.1 < r < 0.4$ pc.

1.3.5 Relativistic collimated jets

Relativistic jets are plasma outflows of energised particles along the rotation axis of the accretion disk or dusty torus. High velocities and relativistically beamed radiation (in the forward direction) are characteristic of these collimated jets. Some elliptical galaxies produce strong radio jets while spiral galaxies produce weak radio jets. A symmetric pair of jets is found mostly associated with parent galaxies of low luminosity, and asymmetry. The sometimes one-sided jet morphology is mostly due to relativistic beaming in the jets. The intensity of the jet is enhanced due to relativistic abberation in the direction of the observer and the intensity of the jet moving in the opposite direction is then lowered to non-detectability [Urry and Padovani, 1995]. Sikora and Madejski [2000] give an overview of jet composition, which sometimes favors a pure leptonic (electrons) particle population in the jet composition. The jet composition can also include hadrons (protons); these are described by hadronic models if the protons are accelerated to ultra-relativistic energies.

1.3.6 The AGN zoo

When speaking of classification of AGN in a nutshell, AGNs are classified based on their radio loudness and their optical spectra and sometimes, if they are present, the angle of the line-of-sight of the observer to the relativistic jet of the AGN. Briefly, the optical and radio classifications will both be discussed. Enormous radio sources with jets usually have elliptical host galaxies and weaker radio sources have spiral host galaxies [Urry and Padovani, 1995]. Optical classification is divided into two types of AGN. Type I AGN and type II AGN are based on the attributes of their ultraviolet and optical spectra. Type I AGN have broad emission lines and bright continua, from hot gas in the gravitational well of the black hole. Type II AGN have narrow emission lines and weak continua. Seyfert galaxies, hosted by spiral galaxies, are divided into two main groups; broad line galaxies (for their broad emission lines) and narrow line galaxies, also called Seyfert 1 and Seyfert 2 galaxies. Most Seyfert 1 galaxies are radio-quiet and fall under type I AGN, with low luminosities, relatively nearby the observer (us, Earth), they are oriented such that the BLR is not obscured by the dusty torus. Radio-quiet Type II AGN are narrow-emission-line galaxies

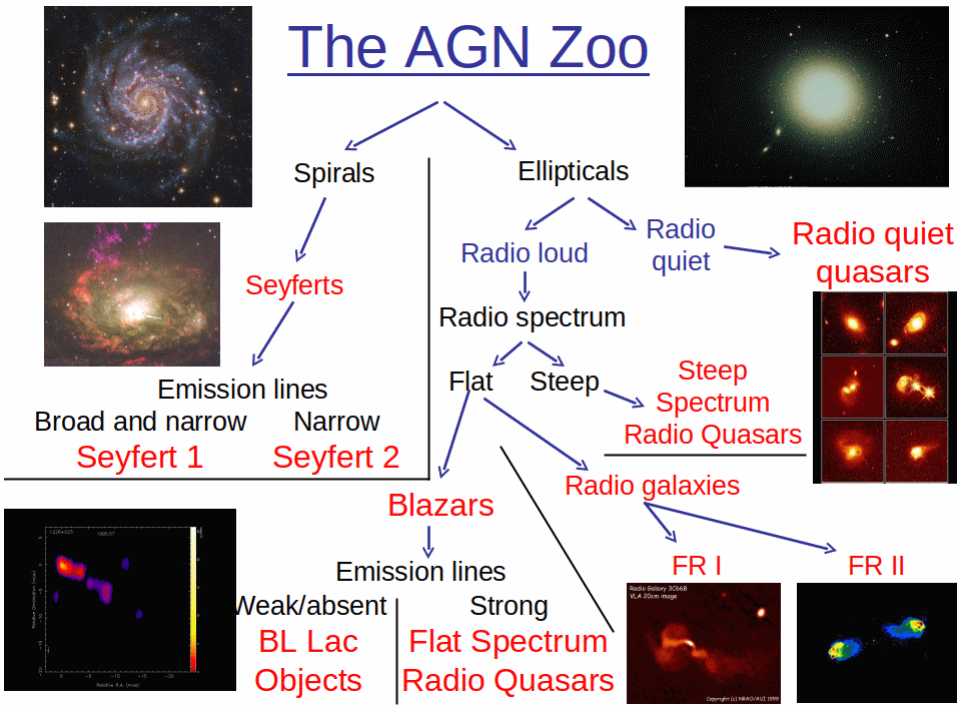

Figure 1.2: The classification system of AGN. From the lecturing notes of Professor Markus Böttcher.

(NELG) and also include Seyfert 2 galaxies with low luminosities; the BLR is obscured by the dusty torus and they are also hosted in spiral galaxies.

AGN hosted by elliptical galaxies are divided into radio-loud and radio-quiet AGN, as illustrated in Figure 1.2. The dusty torus does not obscure the BLR [Urry and Padovani, 1995]. They are more luminous and therefore detectable out to greater distances than Seyfert galaxies. The classification of luminous, radio-loud quasars depends on the radio continuum shape with the line of division set at $\alpha_r = 0.5$. The steep radio spectrum type I AGNs are called steep spectrum radio quasars (SSRQ). The ones with a flat radio spectrum are called Blazars or radio galaxies. The Blazars can be divided into flat spectrum radio quasars (FSRQ) with strong emission lines and BL Lacertae (BL Lac) objects with weak or absent emission lines, as shown in Figure 1.2. Some type II AGNs are narrow-line radio galaxies (NLRG). Flat spectrum radio galaxies have two different morphological types. The Fanaroff-Riley type I radio galaxies (FR I), which are low-luminosity and have radio jets that are often symmetric and whose intensity falls away from the nucleus. Secondly, the Fanaroff-Riley type II radio galaxies (FR II); they have more highly collimated jets and thus more

defined radio lobes with hot spots [Urry and Padovani, 1995].

1.4 Superluminal motion

Superluminal motion refers to the seemingly faster-than-light speeds observed in relativistic jets from blazars and quasars viewed with small viewing angles between our line-of-sight and the jet-axis.

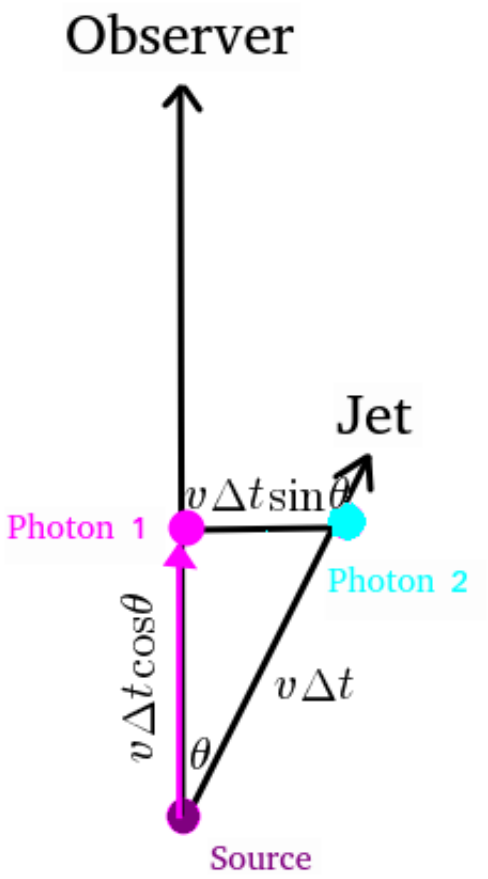

Figure 1.3: A blazar source is emitting a relativistic jet with an angle θ to the observer. Two photons are emitted, at the same angle towards the observer. Photon 1 emitted directly in the observer's line of sight at the source's emission region and photon 2, emitted from the jet at a later stage.

Imagine two photons emitted by this source in Figure 1.3. Photon 1 is emitted at an earlier point in time with respect to photon 2 in the jet and will travel directly to the observer in their line of sight. Photon 2 is emitted at a later point. Photon 1 arrives at Earth (the observers) first, while photon 2 arrives at

a later time. Given the ratio of velocity v and the speed of light c, $\beta = \frac{v}{c}$ and the Lorentz factor, $\Gamma = \frac{1}{\sqrt{1-\beta^2}}$, and using the sketch in Figure 1.3 we can see that the observed velocity seems faster-than-light [Longair, 2011]. The relative time between observing photon 1 and 2, considering light-travel-time effects in general relativity, is:

$$\Delta t_{obs} = \Delta t(1 - \beta \cos\theta) \tag{1.3}$$

The apparent velocity of the emission region perpendicular to the line of sight can be calculated using the basic velocity, distance and time formula:

$$v_{app}^{\perp} = \frac{distance}{\Delta t_{obs}} = \frac{v\Delta t \sin\theta}{\Delta t(1 - \beta\cos\theta)} = \frac{v\sin\theta}{1 - \beta\cos\theta} \tag{1.4}$$

This leads to the general expression:

$$\beta_{app} = \frac{v_{app}}{c} = \frac{\beta\sin\theta}{1 - \beta\cos\theta} \tag{1.5}$$

Taking the derivative of Equation (1.5) with respect to θ:

$$\frac{\partial\beta_{app}}{\partial\theta} = \frac{\beta\cos\theta}{1 - \beta\cos\theta} - \frac{(\beta\sin\theta)^2}{(1 - \beta\cos\theta)^2} = 0 \tag{1.6}$$

$$\beta\cos\theta - \beta^2\cos\theta^2 = \beta^2\sin\theta^2 \tag{1.7}$$

$v_{app}^{\perp}$ is at a maximum when $\cos\theta = \beta$. Equation (1.7) is solved by $\beta = \cos\theta$ and from the definition of the Lorentz factor it is known that $\sqrt{1-\beta^2} = \frac{1}{\Gamma}$ and $1 - \beta^2 = \frac{1}{\Gamma^2}$, which yields:

$$\sin\theta = \sqrt{1 - \cos\theta^2} = \sqrt{1-\beta^2} = \frac{1}{\Gamma} \tag{1.8}$$

and

$$1 - \beta\cos\theta = 1 - \beta^2 = \frac{1}{\Gamma^2} \tag{1.9}$$

Substituting Equation (1.8) and (1.9) into Equation (1.4):

$$v_{app} = \frac{1}{\Gamma}\Gamma^2 v = \Gamma v \tag{1.10}$$

Consequently

$$\beta_{app} = \Gamma\beta \tag{1.11}$$

This proves that the velocity can appear to be faster-than-light.

1.5 Imaging atmospheric Cherenkov telescopes

1.5.1 Atmospheric air showers

Observing very high energy ($100\,GeV - 100\,TeV$) γ-rays is challenging because the atmosphere is opaque to those wavelengths. Telescopes like Fermi-LAT, INTEGRAL and AGILE are mounted on satellites that orbit around the Earth and can observe γ-rays without the hindrance of the atmosphere. Imaging atmospheric Cherenkov telescopes (IACT) are ground-based observatories that detect the Cherenkov light produced by particle air showers caused by γ-rays entering the atmosphere. Cosmic-ray particles also create these extended air showers (EAS) of particles in the same way as γ-rays and constitute a large background to γ-ray detection. Pair production and Bremsstrahlung, as will be explained in Chapter 3, are the two elementary processes that take place [de Naurois and Mazin, 2015]. Figure 1.4 displays the detection process:

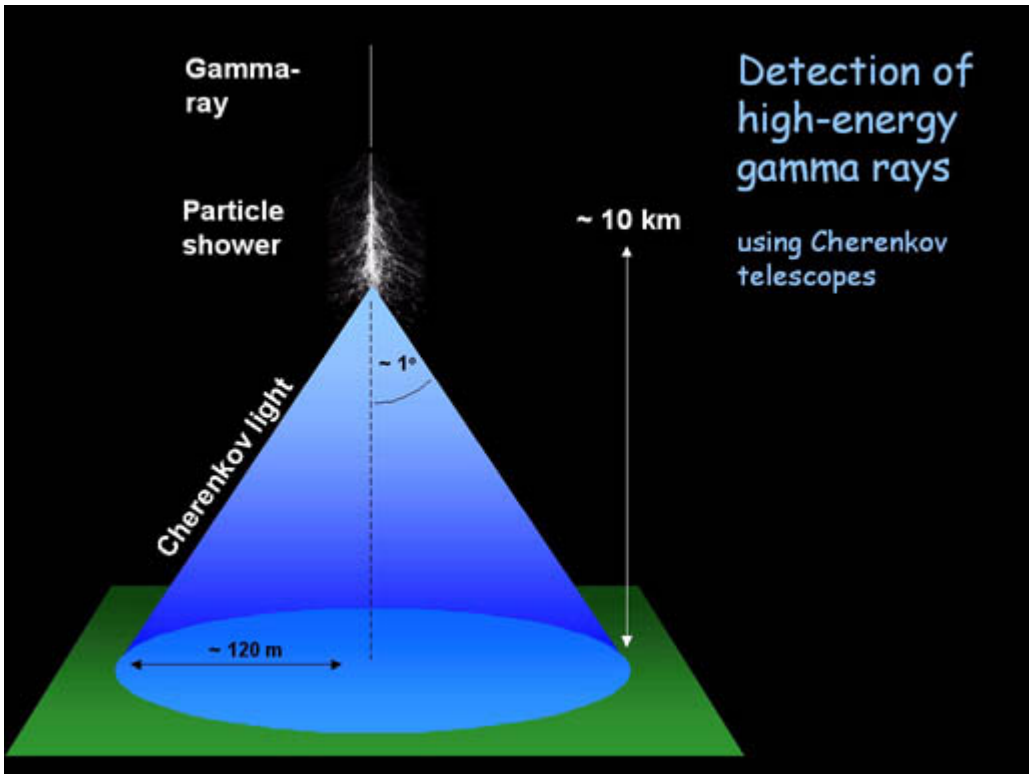

Figure 1.4: A γ-ray enters the atmosphere, interacting with particles in the atmosphere, producing secondary particles which emit Cherenkov light. This information can be found on the H.E.S.S. webpage: https://www.mpi-hd.mpg.de/hfm/HESS/pages/about/telescopes/images/detection2s.jpg.

The Cherenkov light is detected by ground-based Cherenkov telescopes. The orphan flare modeled in this thesis was observed by the HESS telescope.

1.5.2 H.E.S.S. telescope

The H.E.S.S. is located in the Khomas highlands region in Namibia, 1800 m above sea level. The array of five telescopes was constructed in two phases. Phase I consists of four 13 m diameter (107 m^2 mirror area) telescopes called CT1-4, which are arranged in a square with side length 120 m. Phase II was a later addition in 2012 and consists of one 28 m diameter (614 m^2 mirror area) telescope called CT5, in the middle of the square formed by the CT1-4 [1]. CT5 has very fast positioning speed of a 100 degrees per minute and can detect photons with energies from tens of GeV to tens of TeV. The telescopes have Cherenkov detectors that measure the Cherenkov light from particle air showers. See de Naurois and Mazin [2015] and Giebels and H.E.S.S. Collaboration [2013], for an in-depth explanation of how the H.E.S.S. telescope works.

Figure 1.5: The H.E.S.S. site during the day when all the telescopes are safely parked.

1.6 Fermi LAT

Fermi is a γ-ray space telescope that studies the sky at the energy range of 8 keV - 300 GeV, see Figure 1.6. It was launched 11 June 2008 and there are two different instruments on the telescope, the Gamma-ray Burst Monitor (GBM) and the main instrument is the Large Area Telescope (LAT). The Fermi LAT has a larger area and better angular resolution, and field of view than its forerunner, the Energetic Gamma Ray Experiment Telescope (EGRET) and is an imaging γ-ray telescope. In the energy range 20 MeV $-$ 300 GeV, Fermi-LAT observes the primary interaction of photons with the electric field of atomic nuclei that causes the pair production process. As seen in Figure 1.7, incident

[1] https://www.mpi-hd.mpg.de/hfm/HESS/pages/about/

radiation moves through the anticoincidence shield that has a high sensitivity towards charged particles. Then the photons move through thin layers that are called conversion foils, made from high-Z material. Underneath the conversion foils are particle tracking detectors and the energies of the electron and positron produced in the pair-production process are then measured by a calorimeter. The anticoincidence shield works in the following way: it cannot detect photons, thus if there is no detection in the anticoincidence shield but a detection was made by the detectors, it is proof of photons. The conversion foils convert photons because of the heavy nuclei in the foils into electron and positron pairs which are then measured by the particle tracking detectors, and the energies of these pairs are then measured by the calorimeter. All this information is found on NASA's website [2].

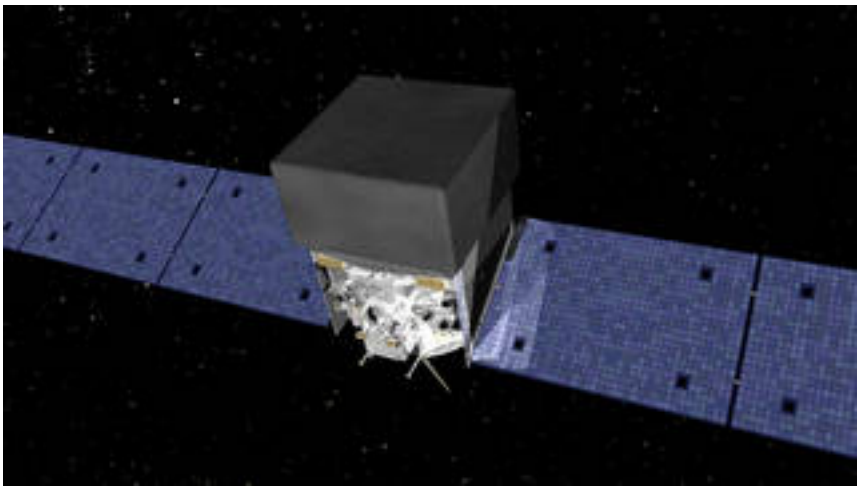

Figure 1.6: Fermi γ-ray space telescope artist concept. Image credit NASA.

[2]https://fermi.gsfc.nasa.gov/science/instruments/lat.html

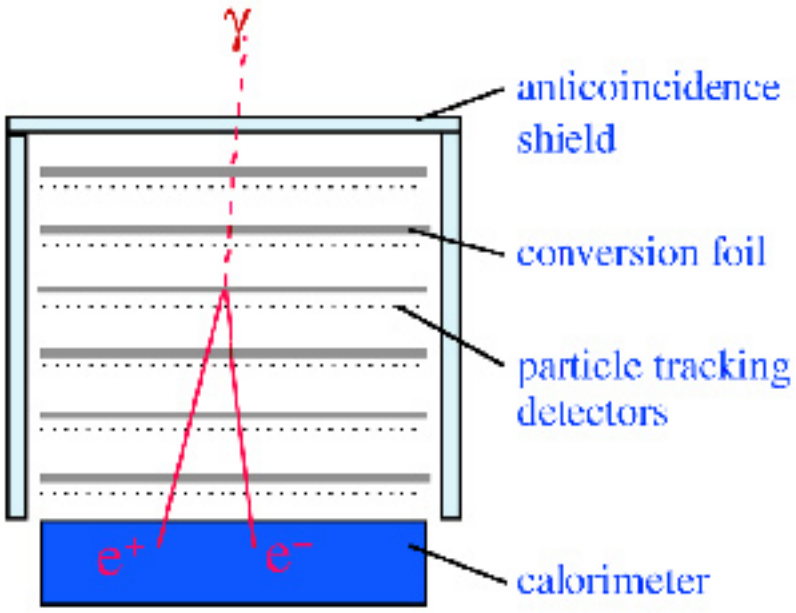

Figure 1.7: The LAT instrument on the Fermi telescope, measuring pair production. This displays the different components of which the LAT instrument consists. Image credit: Aurore Simonnet from the Sonoma State University under the affiliation with NASA.

Chapter 2

Blazar phenomenology

2.1 Spectral energy densities

Spectral energy distributions (SEDs) of blazars display non-thermal emission and radiation components across the electromagnetic spectrum from radio to γ-rays (broad-band continuum). They are usually characterized by two components, a low-energy component and a high-energy component. For both leptonic and hadronic models the low-energy component is produced by electron-synchrotron radiation, in the frequency range from radio - optical or ultraviolet (UV) and sometimes X-rays. In leptonic models the high-energy component (X-rays - γ-rays) is the result of Compton scattering and in hadronic models the high energy photons are produced through proton-synchrotron radiation or photo-pion production, [Böttcher, 2019]. These radiation mechanisms will be discussed in greater detail in Chapter 3.

2.2 The blazar sequence

The blazar sequence is a phenomenological classification of blazars where blazars, BL Lacs and FSRQs, which are most powerful have relatively small synchrotron peak frequencies, ν_{peak}, and the weakest blazars have the highest ν_{peak} values. BL Lac objects have a large range of synchrotron peak frequencies and are divided into low-energy peaked BL Lacs (LBL), ν_{peak} in the infrared (IR) or optical bands and intermediate BL Lac objects (IBLs) with synchrotron frequencies in the optical, and high-energy peaked BL Lacs (HBL), ν_{peak} in the UV or X-ray bands. FSRQs are different, they are only low-energy peaked, there are no high-energy peaked FSRQs, [Padovani, 2007].

The blazar sequence was posited by [Fossati et al., 1998] (F98) and [Ghisellini et al., 1998]. ν_{peak} was plotted for three blazar samples with 126 blazars of which 33 blazars were detected by EGRET. The blazar sequence was originally only the function of one parameter, namely the bolometric luminosity. It was apparent that the most powerful sources (highest luminosities) had the smallest ν_{peak} values and the weakest sources (lowest luminosities) had the highest ν_{peak} values [Fossati et al., 1998] as seen in Fig. 2.1. The mechanism responsible

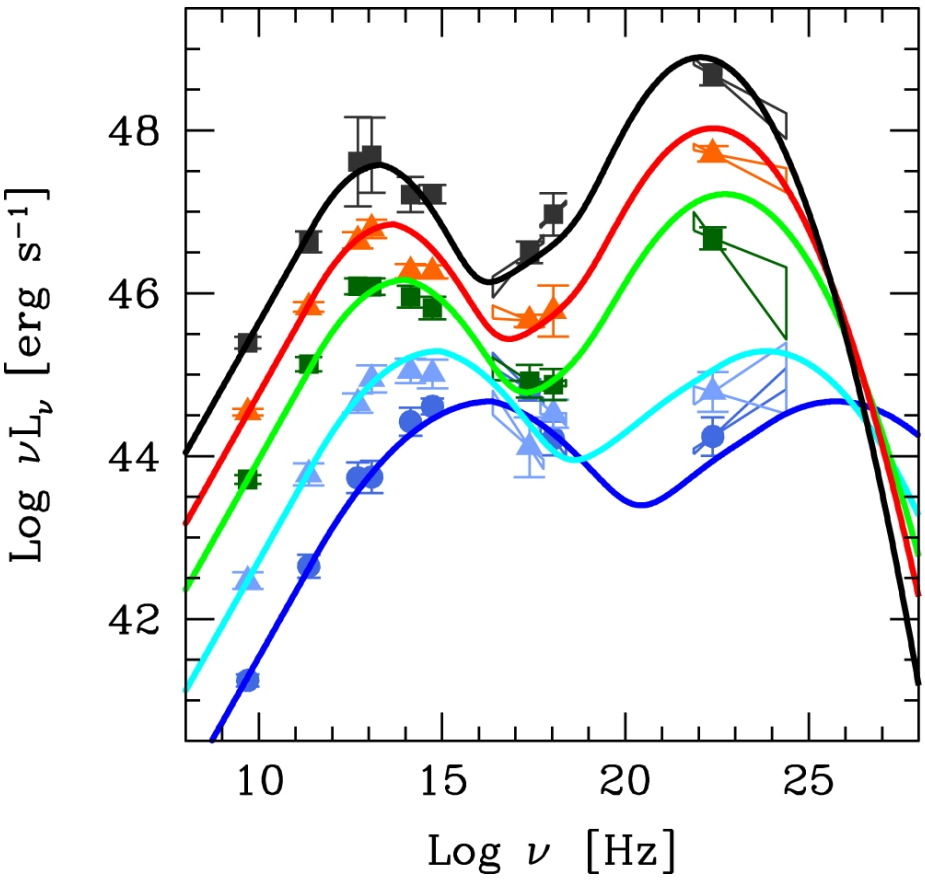

Figure 2.1: The original blazar sequence. The 126 blazars are from X-ray and radio flux-limited samples [Ghisellini, 2016]. The blazars with lower L values have higher synchrotron peak frequencies.

for the high-energy radiation in the blazar sequence is assumed to be inverse Compton scattering in [Fossati et al., 1998]. The synchrotron frequency peak is related to electron energy in the following manner:

$$\nu_{peak} \propto B\delta\gamma_{peak}^2 \tag{2.1}$$

with B the magnetic field, δ the Doppler factor and γ_{peak} the electron energy at the synchrotron frequency peak. In the most powerful sources the energy density is higher and leads to stronger radiative cooling, consequently, the lower ν_{peak} values are achieved and Compton cooling dominates because these blazars typically have a Compton dominance > 1. The blazar sequence is seen as a controversial subject and it is debated whether it is a result of selection effect because of the flux limited samples that are selected. In [Ghisellini, 2016] a new and improved blazar sequence (version 2.0) is investigated. It is found that the blazar sequence has the same overall properties as originally posited. The biggest difference in version 2.0 of the blazar sequence is that the Compton dominance in powerful blazars is found to be less.

2.3 Polarization properties

Polarization is a powerful tool in the multiwavelength studies of blazars. A lot of information is gained by knowing the polarization degree (Π), and the polarization angle (PA). Optical polarization measurements can give us information on the magnetic field structure in the emission region, which can help us understand which radiation mechanisms are present in the relativistic jet of a blazar and determine which models should be applied. Observations of large swings in PA ($\geq 180^{\o}$) that occur simultaneously with γ-ray emission have been interpreted as a signature of a helical magnetic field structure, but there are also alternative explanations (such as the TEMZ model by Marscher [2013]). A study on 191 extragalactic radio jets was made using multifrequency VLBA observations over 12 epochs by the MOJAVE group. They observed transverse gradients in the rotation measure (RM), meaning this also could be evidence for a helical magnetic field. Therefore there is evidence for a toroidal magnetic field component [Blandford et al., 2019]. In 3C279 signs of circular polarization in the core region were observed over a span of 14 years and 20 epochs, as mentioned in Blandford et al. [2019]. Polarization in the low-energy component of blazars is indicative of synchrotron radiation [Romero et al., 2017]. The polarization degree for blazars in the low-energy regime ranges from few to tens of percent, in agreement with what is predicted for synchrotron radiation. X-ray and γ-ray polarization in blazars can determine if leptonic or hadronic γ-ray emission is taking place, [Zhang and Boettcher, 2013]. The polarization degree and angle is significantly variable in the radio - optical range [Böttcher, 2019]. It has been found, however, that very big and speedy rotations of the PA of the electric vectors in some AGN are actually correlated with γ-ray flares, [Blinov et al., 2018].

2.4 Variability

Flux variability is seen in blazars throughout the entire electromagnetic spectrum from time scales of years down to minutes [Aharonian et al., 2007]. One of the unexplained phenomena is that variability across all wavelengths does not show consistent correlation or non-correlation. The shortest scale variability (on scales of minutes) is usually seen in very-high-energy γ-ray emission, detected by ground-based IACTs. Through causality arguments, the variability time scale limits the size of the emission region as seen later in Eq. (4.30) [Böttcher, 2019]. Observed flux variability can also constrain upper limits on the gravitational radius and therefore the BH mass [Barkov et al., 2012]. Hayashida et al. [2012] expands on the multiwavelength variability of 3C279 over the period of August 2008 to August 2010. During this specific time period an apparent correlation of variability in the γ-ray and optical wavebands was observed with a lack of correlation in the X-ray waveband. They used a one-zone model assuming an optical and gamma-ray emission region located a few pc away from the SMBH. They also show, however, that these results can be replicated with γ-ray and optical emission that is produced much closer to the SMBH. Kim et al. [2020] did a more recent very long baseline interferometry (VLBI) study on 3C279 and found rapid broadband flux variability across the entire electromagnetic spectrum of 3C279.

2.5 Orphan flares

Orphan flares are signified by flaring in one waveband unaccompanied by flaring in any other band, and are thus a stand-alone spike in flux. Extreme variability in different wave bands and high-energy flaring are characteristics that are often paired with orphan flares. Orphan flares sometimes are secondary flares that follow after a primary flare seperated a few days in time [Böttcher, 2005]. An example of an orphan flare can be seen from Figure 2.2, taken from the paper [Krawczynski et al., 2004], which was the first orphan flare ever detected on the 4th of June 2002. Orphan flares are still a mystery as there have not been many orphan occurances or studies done on them. A model for an orphan flare event can be found in the paper by [Böttcher, 2005]. Papers on other possible orphan flare models are: Potter [2018] with a time-dependent fluid jet emission model and MacDonald et al. [2017] with the ring of fire model.

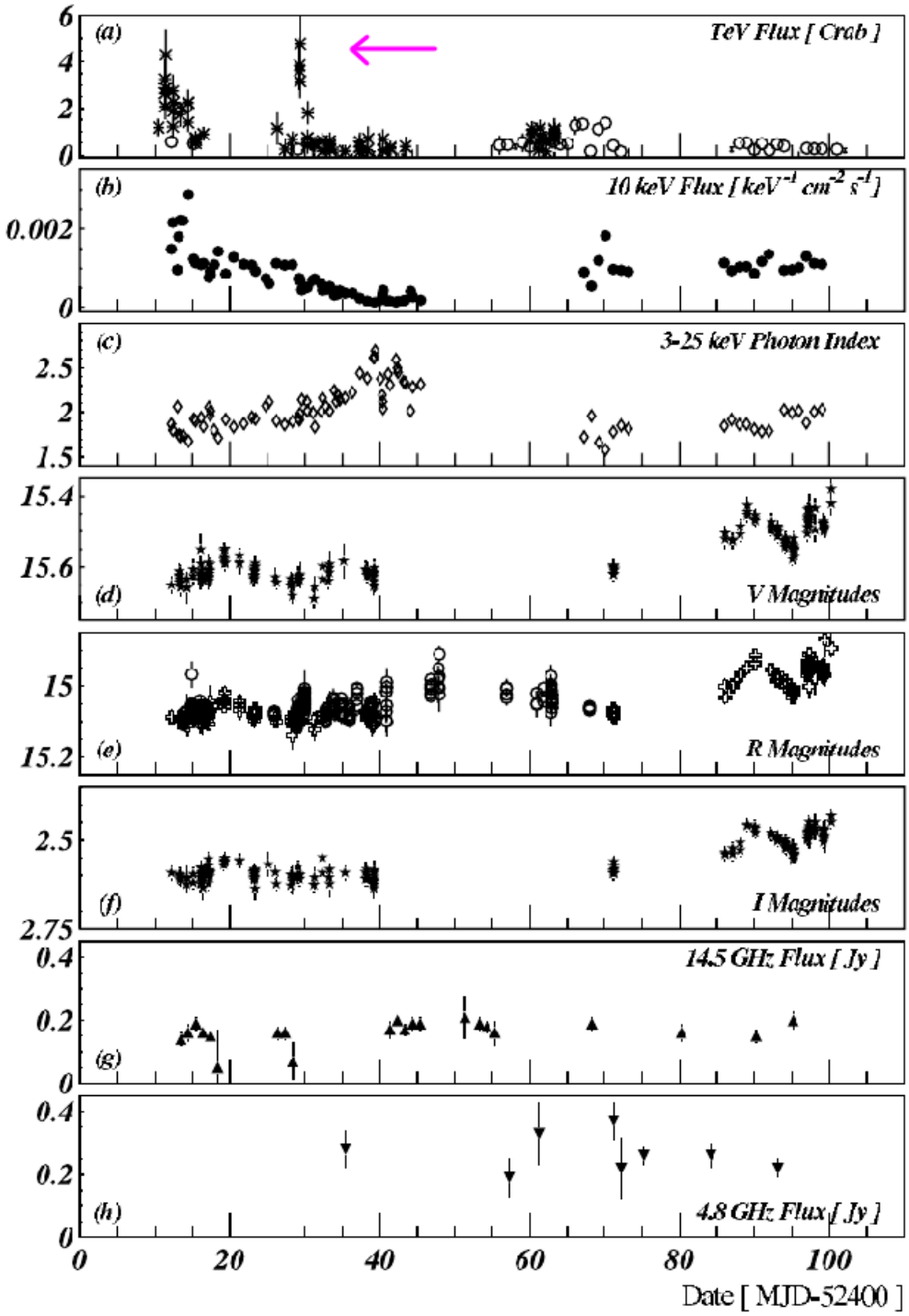

Figure 2.2: Results from the paper of Krawczynski et al. [2004], from the multiwavelength campaign on 1ES 1959+650. There is a primary flare in the TeV and 10 keV bands and then a secondary orphan flare in the TeV band 20 days later, pointed out by a magenta arrow.

Orphan flares are most commonly detected at TeV energies, but can be detected at lower energies as well. Orphan flares have to be caused by different processes than normal $\gamma-$ray flares, which are typically broad-band flares, characterised by variability across the entire electromagnetic spectrum. The first detected orphan flare as mentioned above was detected at TeV energies and was modeled with a synchrotron self Compton (SSC) model [Krawczynski et al., 2004]. Leptonic models have a problem reproducing the TeV γ-ray flare without a simultaneous X-ray flare. Kusunose and Takahara [2006] suggests a structured leptonic jet model for the 2002 orphan flare, where there are multiple dense regions in the jet. The ring of fire model was applied to a γ-flare (0.1-200 GeV) from PKS 1510-089 in 2009 from within one of its inner knots [MacDonald et al., 2017]. A broadband modelling study was done on orphan γ-ray flares that were observed in the blazars, 3C273, PKS 1510-089 and 3C279, [Patel et al., 2021]. From the SED modelling they gather that there are two emission regions, one closer to the base of the jet in the BLR or dusty torus region and one further along the jet. The orphan γ-ray flares seem to originate from the first emission region. One of the objectives of the Kapanadze et al. [2014] study is to investigate the orphan X-ray flare from PKS 2155-304 that ocurred during the August - October period in 2010. They posit that this flare suggests different electron populations in the jet. During a multiwavelength campaign on Mrk 421 in December 2002 and January 2003 an Orphan X-ray flare was discovered and was modelled with an SSC model using high Doppler factors and low magnetic field values. Most papers mentioned above posit the emission region to be close to the base of the jet. We do not really see orphan flares in lower energies, i.e., radio-optical, where the emission is posited to be produced further down in the jet, [Patel et al., 2021].

2.6 3C 279 multiwavelength studies

3C 279 is a galaxy and blazar known by many names: WISE J125611.17-054721.5, [HB89] 1253-055, 4C -05.55 and PKS 1253-05. 3C 279 is located at a right ascension and declination (RA Dec) of $(194.046527°, -5.789312°)$ and a galactic longitude (Lon) and latitude (Lat) of $(305.104299°, 57.062412°)$, [Johnston et al., 1995]. This blazar has an SMBH with a mass that is estimated at about (3-8) $\times 10^8 M_\odot$ [Gu et al., 2001, Woo and Urry, 2002]. 3C 279 is an FSRQ with a redshift of $z = 0.536$, [Lynds et al., 1965], about 2375.85 ± 166.32 Mpc away, [Marziani et al., 1996]. 3C 279 was first detected in the mid 1960's in the optical band [Sandage and Wyndham, 1965]. Emission from 3C 279 has been detected across the electromagnetic spectrum from radio to VHE gamma-rays. 3C 279 is extremely variable across the electromagnetic spectrum. The γ-ray flux above 100 MeV varies across two orders of magnitude, from $\sim 10^{-7}$ to $\sim 10^{-5}$ph cm^{-2} s^{-1} according to Wehrle et al. [1998b] and Maraschi et al. [1992].

3C 279 is most well known for its emission at high energies. Numerous multiwavelength studies have been performed on 3C 279 see: [Maraschi et al., 1994,

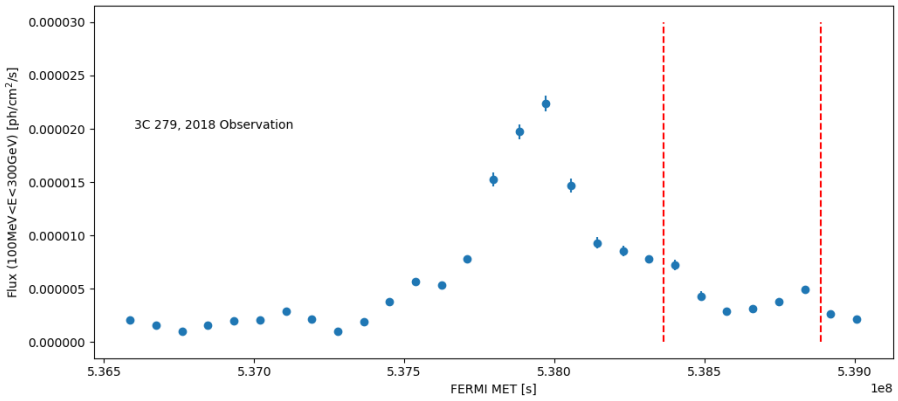

Figure 2.3: The Fermi-LAT light-curve of GeV gamma-rays, for the flare from 3C 279 in January 2018, as per Atel #11239. The H.E.S.S. data were taken during the period bounded by the vertical red lines. The second red line indicates the orphan flare detection. There are 11 days between the Fermi LAT and the H.E.S.S. flare.

Wehrle et al., 1998b, Larionov et al., 2008, Hayashida et al., 2012, Paliya et al., 2015]. 3C 279 is the first γ-ray blazar discovered by EGRET in 1991 [Hartman et al., 1992], and also the first FSRQ seen in very high energies (VHE, $E > 100$ GeV) by the Major Atmospheric Gamma-ray Imaging Cherenkov (MAGIC) telescope [Albert et al., 2008]. In 2009, during a γ-ray flare there was a change in optical polarization correlated with the flare [Fermi-LAT, 2010]. 3C 279 is bright in X-rays and γ-rays. In 2012, there were two orphan X-ray flares from 3C 279 [Hayashida et al., 2012], with a 90-day period in between the two flares. The optical and γ-ray counterparts were so weak that these two flares were seen as isolated. Studying 3C 279 at radio wavelentghs reveals a compact core and very long baseline interferometry (VLBI) reveals superluminal motion [Lister et al., 2013], with apparent superluminal velocities in range of 4-20 c in the jet which is very closely aligned to the line of sight, up to 2^{deg} [Jorstad et al., 2004]. Kim et al. [2020] studied the jet of 3C279 at 1.3 mm (230 GHz) to resolve its features in April of 2017. 3C 279 has a compact core and a straight jet extended from sub-parsec to kilo-parsec scales. That study found substructures in the millimeter VLBI core suggesting a linear, knotty structure or it can be interpreted as a bent jet, possibly due to plasma instabilities. They also found that the jet core is either optically thin at 230 GHz or 3C279 is dominated by magnetic energy if the synchrotron turn-over frequency is close to 230 GHz.

2.6.1 3C 279 Orphan VHE γ-ray flare

On 28 January 2018, H.E.S.S. detected an orphan TeV γ-ray flare in 3C 279. Eleven days before this flare there was a primary flare in the Fermi-LAT range that triggered the observations of 3C 279.

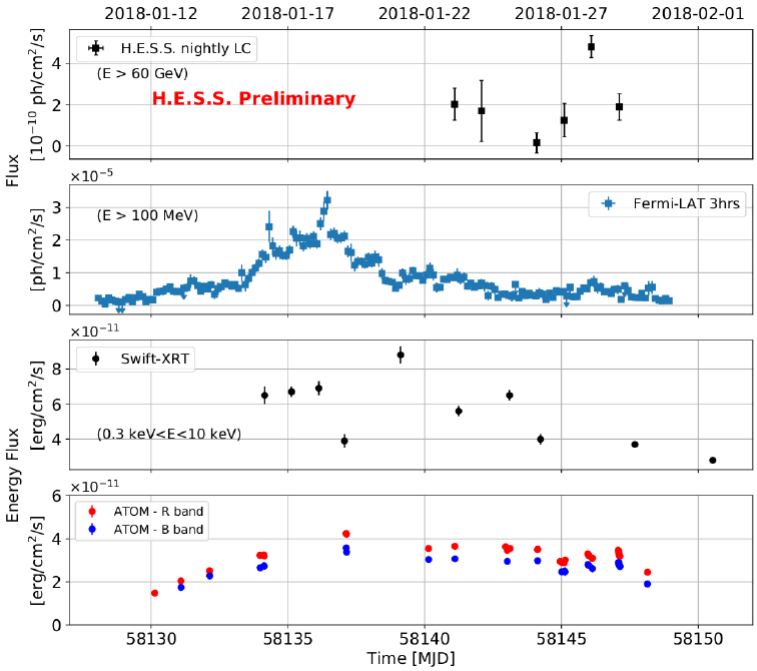

Figure 2.4: The multiwavelength light curves of 3C 279 during its flaring state in January 2018. The top panel denotes the H.E.S.S. light curve above 60 GeV. The second to top panel is the Fermi-LAT light curve above 100 MeV, the second to bottom panel is the Swift-XRT light curve in the range 0.3 - 10 keV and the bottom panel shows the ATOM optical light curve in the R- and B-band [Dmytriiev, 2020].

Figure 2.3 shows the Fermi-LAT light-curve and the H.E.S.S. observation window while 3C 279 was flaring. H.E.S.S. has a Target of Opportunity (ToO) program, where other instruments observing across all wavebands in the electromagnetic spectrum share information for good multiwavelength coverage. Fermi-LAT detected the flaring state of 3C 279 in January 2018 and triggered follow-up observations by H.E.S.S.

In Figure 2.4 it is seen that there is a seven-day delay, between the Fermi-LAT flare and the start of H.E.S.S. observations after the primary Fermi-LAT flare, this was due to bad weather. It is also notable that the primary flare also exhibits flaring in both the Swift and ATOM bands, while the secondary flare on 28 January is an orphan flare. The Hadronic Synchrotron Mirror Model will be investigated in this study, to see if it can provide a consistent explanation for this orphan flare.

Chapter 3

Theoretical background

There are many different mechanisms that accelerate particles in space that cause electromagnetic emission. In this chapter, the focus will be on non-thermal emission. The different radiation mechanisms in leptonic and hadronic models are also discussed. From section 2.1, we know that the low-energy component in blazars is produced by synchrotron radiation discussed in section 3.2.1, the sections thereafter concentrate on the high-energy components of leptonic and hadronic models.

3.1 Non-thermal emission

Non-thermal emission takes place when the particles in the source have a non-thermal energy distribution. Examples of non-thermal emission are synchrotron radiation, Compton scattering and stimulated emission. In the next section, we will be giving a short description of synchrotron radiation and Compton scattering for the leptonic models while, for the hadronic models, we will be discussing proton-synchrotron radiation and photo-pion production. Photo-pion production leads to the production of gamma-rays, muons, positrons, and neutrinos.

3.2 Radiation mechanisms

The Universe is permeated by magnetic fields (**B**) that accelerate particles when they move through these fields. The simplest example is cyclotron radiation. Nonrelativistic electrons that move perpendicular to a magnetic field start gyrating along the magnetic field lines and are thus accelerated [Rybicki and Lightman, 2008]. The frequency of emission is given simply by the frequency of gyration.

The cyclotron frequency is found by balancing the Lorentz and centripal forces:

$$\frac{\gamma m_e v^2}{r} = q|\vec{v} \times \vec{B}| = \frac{v}{c} eB \sin(\alpha) \tag{3.1}$$

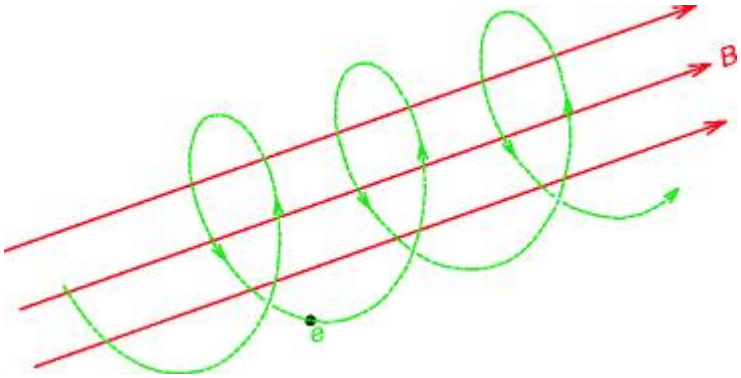

Figure 3.1: The Lorentz force that acts on a particle (electron) with charge, e, which is moving non-relativistically or relativistically with a velocity **v**, causes the particle to gyrate with a specific radius around the magnetic field lines, **B**

where γ is the Lorentz factor, m_e is the mass of the electron, v is the velocity of the electron and r is the gyration radius, while $q = e$ represents the charge of the electron, c is the speed of light, and B is the magnetic field with α the angle between the direction of motion of the electron and the magnetic field lines. Simplifying equation (3.1), we find:

$$\frac{\gamma m_e v}{r} = \frac{eB\sin(\alpha)}{c} \tag{3.2}$$

The cyclotron frequency is calculated using the gyration frequency of the particle. The path travelled during one gyration is the same as the circumference of the gyration, $\lambda = 2\pi r$ and consequently the gyration frequency can be calculated using the general formula for frequency, $\nu = \frac{v}{\lambda}$:

$$\nu_{gyr} = \frac{eB\sin(\alpha)}{2\pi\gamma m_e c} \tag{3.3}$$

For non-relativistic electrons $\gamma \approx 1$, the cyclotron frequency is then given by:

$$\nu_{cy} = \frac{eB}{2\pi m_e c} \approx 2.8 \times 10^6 \left(\frac{B}{G}\right)\ Hz \tag{3.4}$$

Cyclotron radiation gets mostly absorbed, emissivity in cyclotron radiation is very small, but electrons can be efficient in absorbing incoming radiation at the characteristic cyclotron frequency. The following sections concentrate on relativistic particles.

3.2.1 Synchrotron radiation

A general discussion of synchrotron radiation is described in this section, where we will be using electrons for our particles to describe electron-synchrotron radiation, but all the masses can be replaced by m_p, the proton mass and then

proton-synchrotron radiation is described. Synchrotron radiation is basically the same as cyclotron radiation with relativistic electrons. It is, however, a bit more complex and extends to many times the gyration frequency [Rybicki and Lightman, 2008]. Taking into account that the electrons are now moving with relativistic speeds, the velocity is $v = \beta c \approx c$, because for relativistic electrons $\beta \approx 1$. The electron, radiating towards Earth, must be moving in the direction of Earth, an observer from Earth sees it as it covers an angle of $\frac{1}{\gamma}$, the beaming cone of the radiation, along the gyration motion. Therefore, the time observed is:

$$\Delta t_{obs} = \frac{1}{\nu_{gyr}\gamma}(1-\beta) \tag{3.5}$$

where $1-\beta$ is the correction factor for the electron keeping up with emission it just radiated. The equation is simplified:

$$\Delta t_{obs} = \frac{1}{\nu_{gyr}\gamma}(1-\beta)\frac{(1+\beta)}{(1+\beta)} = \frac{1}{\nu_{gyr}\gamma}\frac{(1-\beta^2)}{(1+\beta)} \tag{3.6}$$

where $(1-\beta^2) \approx \gamma^{-2}$ and $(1+\beta) \approx 2$. Thus:

$$\Delta t_{obs} = \frac{1}{2\nu_g\gamma^3} \tag{3.7}$$

We know that the synchrotron frequency is given by the inverse of the observed period and using equation (3.3):

$$\nu_{sy} = \frac{1}{\Delta t_{obs}} = 2\nu_g\gamma^3 = \frac{eB\sin\alpha\gamma^2}{\pi m_e c} \tag{3.8}$$

where $\frac{eB\sin\alpha}{\pi m_e c} = \nu_0 = 4.2 \times 10^6 \frac{B}{G}\sin\alpha\ Hz$.

The total radiated power due to synchrotron radiation is given by:

$$P = \left(\frac{dE}{dt}\right) = \frac{4}{3}c\sigma_T u_B(\gamma\beta)^2 \tag{3.9}$$

where $\sigma_T = 6.65 \times 10^{-25}\ cm^2$ is the Thomson cross-section and u_B is the magnetic energy density. The derivation for the energy loss rate can be found in Rybicki and Lightman [2008]. The synchrotron cooling time scale is given by:

$$t_{syn} = \frac{E}{\left(\frac{dE}{dt}\right)} = \frac{3m_e c^2}{4c\sigma_T u_B \gamma\beta^2} \tag{3.10}$$

3.2.2 Leptonic models

Leptons are dominant in leptonic models for blazars, and therefore the radiative output in these models is dominated by electrons and electron-positron pairs. In the case of there being any protons present in the outflow of the jet, they are not accelerated to high enough energies and do not contribute significantly to the radiative output. High energy emission is then best explained by Compton scattering [Böttcher et al., 2013].

Compton scattering

Compton scattering was discovered by Arthur Holly Compton and is simply explained as an incident photon scattering off an electron at rest, resulting in the scattered photon having less energy than before the scattering and the electron experiences recoil. Compton scattering is an example of inelastic scattering. In the electron rest frame:

$$\epsilon_f = \frac{\epsilon_i}{1 + \epsilon_i(1 - \cos\chi)} \tag{3.11}$$

where χ is the scattering angle between the incident photon and the direction of the scattered photon, the dimensionless energy is given by:

$$\epsilon = \frac{E_{ph}}{m_e c^2} = \frac{h\nu}{m_e c^2} \tag{3.12}$$

The limits of Compton scattering are given by the Thomson and Klein-Nishina regime. Thomson scattering is an example of elastic scattering where the incident and final energy are approximately the same $\epsilon_i \approx \epsilon_f$, where ϵ is the dimensionless photon energy. Thomson scattering only occurs at low energies (low frequencies), $\epsilon \ll 1$. The Klein-Nishina regime is in high energies (high frequencies), $\epsilon_i \gg 1$ where $\epsilon_f \approx 1$. There is a quantum mechanical calculation for the cross-section [Jauch and Rohrlich, 1976]. Asymptotic limits for the cross-section in the Thomson and Klein-Nishina regimes are given by:

$$\sigma_c(\epsilon) = \sigma_T \left(1 - 2\epsilon + \frac{26}{5}\epsilon^2\right) \; for\; \epsilon \ll 1 \tag{3.13}$$

$$\sigma_c(\epsilon) = \frac{3}{8}\frac{\sigma_T}{\epsilon}(ln[2\epsilon] + 0.5) \; for\; \epsilon \gg 1 \tag{3.14}$$

The Klein-Nishina formula is a representation of the differential cross-section for unpolarised radiation and is given by:

$$\frac{d\sigma}{d\Omega} = \frac{r_0^2}{2}\frac{\epsilon_f^2}{\epsilon_i^2}\left(\frac{\epsilon_i}{\epsilon_f} + \frac{\epsilon_f}{\epsilon_i} - \sin\chi^2\right) \tag{3.15}$$

As the photon energy becomes large, the Klein-Nishina effect reduces the cross section to values smaller than the Thomson cross section; at high energies, Compton scattering becomes less efficient [Rybicki and Lightman, 2008].

Inverse Compton scattering refers to incident relativistic electrons scattering off photons; the electrons lose their energy to the photons. It is called inverse Compton scattering because the electrons and not the photons lose their energy. If the source of the seed photons for the Compton scattering process is within the jet, it is referred to as synchrotron self-Compton (SSC). However, if the source of the seed photons is in an external field, like the BLR or accretion disk regions, it is called external Compton (EC) [Wehrle et al., 1998a]. Considering the upscattered frequencies of the photons the energy gain can be estimated as:

$$\nu_{ph} \propto \gamma^2 \nu_0 \tag{3.16}$$

To explain the quadratic nature of the energy gain we need to consider Compton scattering in the electron rest frame (primed values), as well as in the laboratory frame. The photon energy in the electron rest frame $\epsilon^{'}$ is related to the laboratory frame photon energy by the following equation:

$$\epsilon^{'} = \epsilon\gamma\left(1 - \beta\mu\right) \tag{3.17}$$

where $\mu = \cos\theta$ and θ is the scattering angle of the photon. The laboratory frame energy is related to the electron rest frame energy by the following expression:

$$\epsilon_S = \epsilon_S^{'}\gamma\left(1 + \beta\mu_s^{'}\right) \tag{3.18}$$

where $\mu = \cos\theta_S^{'}$ and $\theta_S^{'}$ is the scattering angle of the electron. Considering the Thomsom regime, the scattering in the electron rest frame will be elastic, this means that: $\epsilon_S^{'} \sim \epsilon_S$. In the laboratory frame it is found that: $\epsilon_S \sim \gamma^2\epsilon$. This is explained in the book by Böttcher et al. [2012] more thouroughly. This was just a brief introduction to leptonic models, next hadronic models are discussed.

3.2.3 Hadronic models

In hadronic models, the relativistic jet composition consists of protons and electrons that are accelerated relativistically along the jet. The emission processes in hadronic models are proton-synchrotron radiation and/or photo-meson production that causes subsequent synchrotron-pair cascades. External photon fields will act as a target field for protons to interact with or internal fields produced by co-accelerated electrons [Mücke et al., 2003]. Hadronic models in blazars are a plausible source of extragalactic neutrinos; neutrinos are produced by photo-pion production.

Proton-synchrotron radiation

For protons to contribute significantly in radiative emission through proton synchrotron radiation, they need to be accelerated to energies of $E_p = E_{19}10^{19}eV$ where $E_{19} \geq 1$ for observable fluxes to be produced. Protons are 1836 times heavier than electrons, and a magnetic field of $\geq 10\ G$ is needed for protons to be accelerated to relativistic energies [Mücke et al., 2003], because the protons' Larmor radius must be smaller than the emission-region size. Proton-synchrotron models for blazars require jet powers in the range of $10^{47} - 10^{49}\ erg.s^{-1}$ [Böttcher et al., 2013].

Bethe-Heitler pair production

Bethe-Heitler pair production describes the process where electron-positron pairs are created by a photon interacting with a proton (see Figure 3.2).

$$p + \gamma \rightarrow p^{'} + e^{+} + e^{-} \tag{3.19}$$

The energy threshold condition for Bethe-Heitler pair production can be derived using energy and momentum conservation principles and is given by the following equation:

$$E_{thr} = \frac{2m_e(m_e + m_p)c^4}{(1 - \beta_p \mu)E_{ph}} \tag{3.20}$$

Figure 3.2 is a visual representation of the Bethe-Heitler pair production.

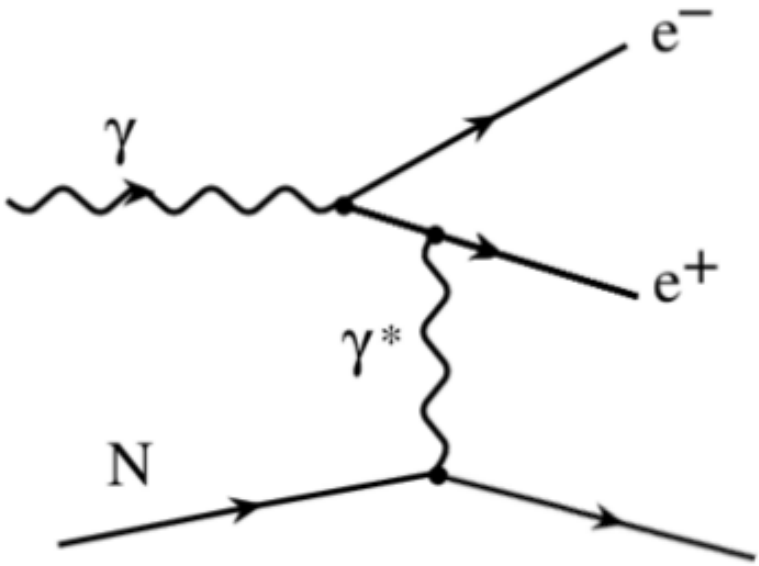

Figure 3.2: Feynman diagram of the Bethe-Heitler process [Dmytriiev, 2020]

Photo-pion production

For photo-meson interactions to take place, the threshold energy for photo-meson interaction needs to be exceeded. When speaking of mesons in photo-meson productions, we are referring mainly to pions. The threshold energy in the cm-frame can be calculated using the conservation of momentum principle. For an example of how to calculate threshold energy consider the first part of the photo-pion interaction in equation (1.2):

$$p + \gamma \rightarrow p + \pi^0 \tag{3.21}$$

The four-momentum of the particles in equation (3.21) is given by:

$$\underline{p}_{p,\pi} = \gamma m_{p,\pi} c \begin{bmatrix} 1 \\ \vec{\beta}_{p,\pi} \end{bmatrix}; \quad \underline{p}_{ph} = \frac{E_{ph}}{c} \begin{bmatrix} 1 \\ \vec{k} \end{bmatrix} \tag{3.22}$$

where $\vec{k}$ gives the direction of the incident photon with incident angle θ, E_{ph} is the energy of the photon and m_p, m_π are the mass of the proton and pion. Using the principles of conservation of energy and momentum, in the center-of-momentum frame, equation (3.21) is represented by:

$$\underline{p}_{ph} + \underline{p}_{p} = \underline{p}_{p}^{'} + \underline{p}_{\pi} \tag{3.23}$$

Squaring both sides of equation (3.23) yields:

$$\underline{p}_{ph}^2 + 2\underline{p}_{ph}\underline{p}_{p} + \underline{p}_{p}^2 = \underline{p}_{p}^{'2} + 2\underline{p}_{p}^{'}\underline{p}_{\pi} + \underline{p}_{\pi}^2 \tag{3.24}$$

Substituting in equation (3.22), yields:

$$(m_p c)^2 + 2\gamma_p E_{ph} m_p (1 - \vec{\beta_p} \cdot \vec{k}) = (m_p c)^2 + 2\gamma^2 m_p m_\pi c^2 \left(1 - \vec{\beta}_\pi \cdot \vec{\beta}_p\right) + (m_\pi c)^2 \tag{3.25}$$

Simplifying the righthandside (r.h.s.) of equation (3.25), at threshold, in the centre-of-momentum frame where, both particles are produced at rest where $\gamma = 1$ and $\beta = 0$ for all particles:

$$\gamma m_p = \frac{m_\pi m_p \left(1 + \frac{m_\pi}{2m_p}\right) c^2}{E_{ph}(1 - \beta_p \mu)} \tag{3.26}$$

with $\mu = \cos\theta = \vec{k}_1 \cdot \vec{k}_2$. Multiply with c^2 to get energy ($E_p = \gamma_p m_p c^2$) on the lefthandside (l.h.s.) of equation (3.26):

$$E_p^{thr} = \gamma m_p c^2 = \frac{m_\pi m_p \left(1 + \frac{m_\pi}{2m_p}\right) c^4}{E_{ph}(1 - \beta_p \mu)} \tag{3.27}$$

The energy at threshold where $\mu = -1$ with which a proton interacts, in the laborotary rest frame:

$$E_{ph}^{thr} = m_\pi c^2 \left(1 + \frac{m_\pi}{2m_p}\right) \approx \ 145 MeV \tag{3.28}$$

Now, secondary particles can be produced through photo-pion processes [Böttcher et al., 2012].

Photo-pion production is essential for neutrino emission, as can be seen in Equation (1.2). The pion production rate is determined by the cross section. In Figure 3.3 the partial cross-sections for the resonance excitation and decay, direct pion-production, diffractive scattering and multipion production are

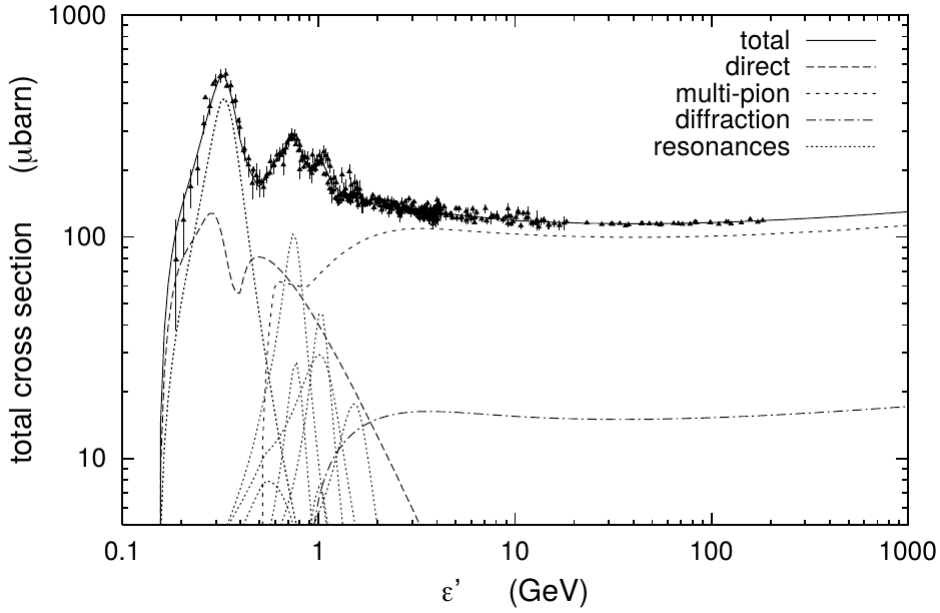

Figure 3.3: The total pγ cross section produced by the SOPHIA Monte Carlo code, version 1.4 [Mücke et al., 2000]. Contributions of baryon resonances, direct photo-pion production, diffractive scattering and multipion production as a function of photon energy in the nuclear rest frame are displayed [Böttcher et al., 2012]. Where $1\mu barn = 10^{-30}\ cm^2$

displayed. The contributions of each interaction are evaluated through their properties of mass, width and decay branching ratios. The Δ-approximation determines the number ratio of photomeson production by using the branching ratios of the delta resonance ($\Delta^+(1232)$), the largest resonance, which dominates the photomeson production [Böttcher et al., 2012]. In the next chapter, the maximum γ_p in the proton energy range is calculated and an analytic calculation estimates if the hadronic synchrotron mirror model is plausible and if there is a dense enough targetphoton field for photo-pion production to take place. More of this process is explained in Chapter 5.4.

Chapter 4

The Mirror Model

In this chapter a detailed analytical approach to the hadronic synchrotron mirror model is presented. This model is essentially a one-zone model with an external photon field, like a gas cloud, reflecting the emission-region's synchrotron radiation.

In Figure 4.1, the very-high-energy bump in the Lepto-hadronic model is due to photo-hadronic processes, which could be enhanced in a synchrotron-mirror scenario. This would lift the third component of the green line, caused by the photo-pion production, to the level of the proton-synchrotron component (2nd bump). The very-high-energy bump is not necessarily a feature occuring because of the orphan flare, but is rather a feature associated with the presence of protons in the jet, dominating the radiation mechanisms. The aim is then to investigate whether it is feasible that a synchrotron mirror scenario may be able to enhance the target photon density sufficiently to produce a flare of the photo-pion-induced radiation component without affecting the proton-synchrotron-dominated Fermi-LAT spectrum. This will be achieved by analytically calculating the energy density from basic principles in section 4.1.1. A second calculation of energy density will be done in section 4.1.2 from energy loss rates, to see what values of energy density are required, in order to produce the observed orphan flare in this scenario. If the two energy densities are similar, the hadronic synchrotron mirror model is feasible.

4.1 Model setup

The Hadronic Synchrotron Mirror Model is studied analytically and numerically. The geometry of the model setup is sketched in Figure 4.2. The emission region moves at highly relativistic speeds, therefore $\Gamma \gg 1$ and thus $\beta_\Gamma \approx 1$. The emission is beamed at a small angle with respect to the observer's line of sight [Romero et al., 2017]; the distance travelled from the emission region by the primary gamma-ray flare to the location of the cloud is given by $R_m = 2\Gamma^2 c\Delta t$, with Δt the observed time delay between primary and orphan flare, where $\Delta t = 11\ days$.

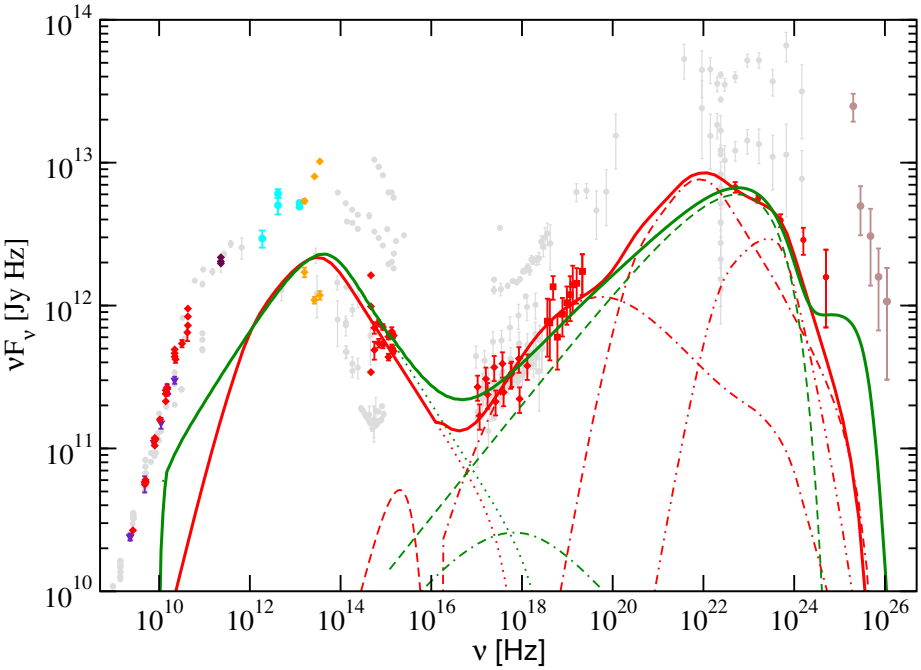

Figure 4.1: Spectral energy distribution of 3C279 with a Lepto-hadronic Model fit, represented by the green line, and a leptonic fit, represented by the red line. This is taken from Böttcher et al. [2013], 3C 279 was in a queiscent state. The lepto-hadronic (green line) fit has three components: the low-energy component caused by electron-synchrotron processes, the high-energy component caused by proton-synchrotron processes, and then a third very-high-energy component caused by photo-pion interaction. Dotted: synchrotron; dashed: accretion disk; dot-dashed: SSC; dot-dash-dashed: EC(disk); dot-dot-dashed: EC(BLR).

As illustrated in Figure 4.2, a blob of relativistic particles (protons and electrons) is propagating at relativistic speeds along the jet. The electron-synchrotron emission from the blob hits a gas cloud (e.g., of the broad line region of the quasar) that acts as a mirror and reflects the synchrotron photons back, which then enter the still emitting jet again, constituting an intense target photon field for photo-pion production ([Böttcher, 2005]). The emission from the source is beamed in a narrow cone with opening angle, $\theta = \frac{1}{\Gamma}$. Basic principles and the Hadronic Synchrotron Mirror Model are used to calculate and integrate over the contributions from all points along the jet starting from the primary flare to the jet-cloud interaction (orphan flare). The assumption that a fraction, τ, of the synchrotron flux from the moving emission region is reprocessed quasi-isotropically by the cloud is made to calculate the target

photon field.

4.1.1 Analytical density calculations from basic principles

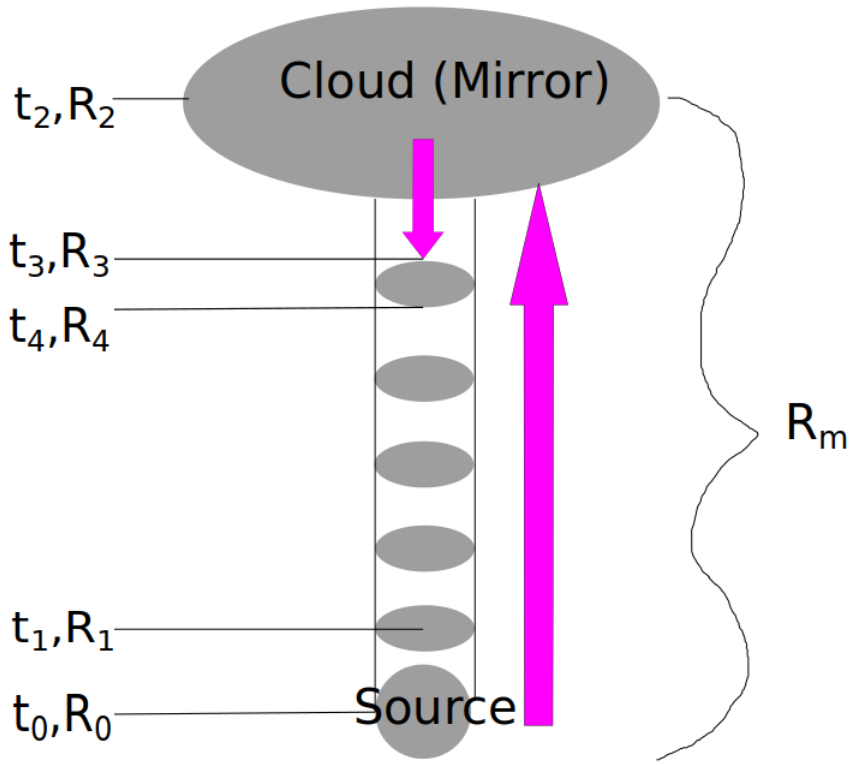

Figure 4.2: Geometry of the model. As from Böttcher [2007] a synchrotron flare is produced in the emission region at time t_1. The synchrotron emission is then reflected when it reaches the cloud, which acts as a mirror. A secondary flare is then produced when the primary synchrotron emission is reflected back into the emission region, at time t_3.

The total distance from the black hole to the cloud is given by R_m. The distance of the emission region from the black hole can be calculated as following:

$$R(t) = R_0 + \beta_\Gamma ct \tag{4.1}$$

The time when the primary synchrotron flare is produced, $t_1 = \frac{R_1}{\beta c}$, is used to calculate t_2, the time the primary synchrotron flare radiation reaches the cloud, which is given by:

$$t_2 = t_1 + \frac{R_m - R_1}{c} \tag{4.2}$$

t_3, the time when the reflected synchrotron radiation hits the emission region, is given by:

$$t_3 = t_2 + \frac{R_m - R_3 - \frac{R_b}{\Gamma}}{\beta c} = t_1 + \frac{R_m - R_1}{c} + \frac{R_m - R_3 - \frac{R_b}{\Gamma}}{\beta c} \tag{4.3}$$

The term $\frac{R_b}{\Gamma}$ includes the size of the blob moving along the jet. The time duration of the primary flare to the secondary flare from observations will be influenced by the light-travel-time effect of $D \approx \frac{1}{2\Gamma^2}$:

$$t_{obs} \approx (1-\beta)t \approx \frac{t}{2\Gamma^2} = \frac{R_m}{2\Gamma^2 c} \tag{4.4}$$

From equation (4.1), we know that:

$$R_{1,3} = R_0 + \beta c t_{1,3} \tag{4.5}$$

Substituting (4.5) into t_3, yields:

$$t_3 = t_1 + \frac{R_m - R_0 - \beta c t_1}{c} + \frac{R_m - R_0 - \beta c t_3}{\beta c} - \frac{R_b}{\Gamma \beta c} \tag{4.6}$$

Some rearranging yields:

$$t_3 = t_1 \frac{(1-\beta)}{(1+\beta)} + \frac{(1+\frac{1}{\beta})(R_m - R_0)}{c(1+\beta)} - \frac{R_b}{\Gamma \beta c (1+\beta)} \tag{4.7}$$

The emission region is moving at highly relativistic speeds and therefore a few assumptions can be made: $\Gamma \gg 1$ then $\beta \approx 1$ and assume $R_0 = 0$. Then:

$$t_3 = \frac{t_1}{4\Gamma^2} + \frac{R_m}{c} - \frac{R_b}{2\Gamma c} \tag{4.8}$$

t_3 can now be substituted into R_3:

$$R_3 = \frac{\beta c t_1}{4\Gamma^2} + \beta R_m - \frac{\beta R_b}{2\Gamma} \tag{4.9}$$

The fourth time step denotes the reflected particles as they move completely through the approaching blob:

$$t_4 = t_3 + \frac{2R_b}{\Gamma c} \tag{4.10}$$

The radiation energy density at the location of the mirror or the reflecting cloud is calculated in Böttcher [2005] as:

$$u_{cl} = \frac{\nu F_\nu(sy) d_L^2}{(R_m - R_1)^2 c} \tag{4.11}$$

The luminosity is defined as the radiative power output of a source and therefore: $L = \frac{dE}{dt}$, where the total energy is given by the product of the volume and the energy density: $E = \frac{4}{3}\pi R^3 u$. The luminosity of the jet electron synchrotron radiation, scattered isotropically by the cloud, is then given by:

$$L_{cl} = \frac{u_{cl}\tau\frac{4}{3}\pi R_{cl}^3}{\frac{R_{cl}}{c}} = \frac{4}{3}u_{cl}\tau\pi R_{cl}^2 c \tag{4.12}$$

where τ is the fraction of photons that are scattered. The cloud or mirror is now assumed to be a sphere, and therefore the flux of reflected jet synchrotron emission impinging onto the emission region at R_3 can be calculated as:

$$F = \frac{L}{4\pi R^2} \approx \frac{L_{cl}}{4\pi(R_m - R_3)^2} \tag{4.13}$$

Substituting in R_3, rearranging and remembering that $(1-\beta) \approx \frac{1}{2\Gamma^2}$ yields:

$$F = \frac{L_{cl}}{4\pi(R_m - \frac{\beta c t_1}{4\Gamma^2} - \beta R_m)^2} = \frac{\Gamma^4 L_{cl}}{\pi(R_m - \frac{\beta c t_1}{2})^2} \tag{4.14}$$

The relation between flux and energy density is used to calculate the energy density in equation (4.17):

$$F = \frac{dE}{dAdt} \tag{4.15}$$

$$u = \frac{dE}{dV} \tag{4.16}$$

with the volume given by $dV = dA\ c\ dt$. The energy density can be related in these ways:

$$u = \frac{dE}{dAcdt} = \frac{L}{Ac} = \frac{F}{c} \tag{4.17}$$

The energy density of reflected jet synchrotron emission in the emission region at point R_3 in the rest frame of the emission region is given by Böttcher [2005]:

$$u'_{R,sy}(t_1) = \Gamma^2 u_{R,sy} \tag{4.18}$$

Equations (4.14) and (4.17) along with $u_{R,sy}$ can be used to find the following expression:

$$u'_{R,sy}(t_1) = \frac{\Gamma^6 L_{cl}}{\pi(R_m - \frac{\beta c t_1}{2})^2 c} = \frac{4\Gamma^6 u_{cl}\tau R_{cl}^2}{3(R_m - \frac{\beta c t_1}{2})^2} = \frac{4\Gamma^6 \nu F_\nu(sy) d_L^2 \tau R_{cl}^2}{3(R_m - R_1)^2(R_m - \frac{\beta c t_1}{2})^2 c} \tag{4.19}$$

To get the average energy density, accumulated over all locations $R_1(t_1)$ from which jet synchrotron radiation is emitted as the blob travels towards $R_3(t_1)$, this expression needs to be integrated over t_1:

$$\langle u'_{R,sy}\rangle = \int_0^{\frac{R_m-R_b}{\beta c}} \frac{u'_{R,sy}}{\Delta t} dt_1 \tag{4.20}$$

$$\langle u'_{R,sy}\rangle = \frac{4\Gamma^6 \nu F_\nu(sy) d_L^2 \tau R_{cl}^2}{3(R_m - R_b)} \int_0^{\frac{R_m-R_b}{\beta c}} \frac{dt_1}{(R_m - \beta c t_1)^2 (R_m - \frac{\beta c t_1}{2})^2} \tag{4.21}$$

where $\Delta t = \frac{R_m - R_b}{\beta c}$ is the duration over which the reflected synchrotron photons are being received. Let $t_f = \frac{R_m - R_b}{\beta c}$ and $\alpha = \frac{R_m}{\beta c}$, then the integral of this expression is given by:

$$I = \frac{4}{(\beta c)^4} \int_0^{t_f} \frac{dt_1}{(\frac{R_m}{\beta c} - t)^2 (\frac{2R_m}{\beta c} - t)^2} \tag{4.22}$$

$$I = \frac{4}{(\beta c)^4} \int_0^{t_f} \frac{dt}{(\alpha - t)^2 (2\alpha - t)^2} \tag{4.23}$$

Let $x = \alpha - t$ then $\alpha = x + t$ and $t = a - x$ where $dt = -dx$. This yields:

$$I = \frac{4}{(\beta c)^4} \int_{\alpha - t_f}^{\alpha} \frac{dx}{x^2(\alpha + x)^2} = \frac{4}{(\beta c)^4} \int_{x_f}^{\alpha} \frac{dx}{x^2(\alpha + x)^2} \tag{4.24}$$

where $x_f = \alpha - t_f$ is the time for photo-pion interactions to take place. α is the time it takes the blob to move to the centre of the cloud, and t_f is the total integration time. The standard integral solution to this integral, is:

$$I = \frac{4}{(\beta c)^4} \left[- \left(\frac{2}{\alpha^2[\alpha + x]} + \frac{1}{\alpha x[\alpha + x]} - \frac{2}{\alpha^3} \ln\left(\frac{\alpha + x}{x}\right)\right)\right]_{x_f}^{\alpha} \tag{4.25}$$

This simplifies to:

$$I = \frac{4}{(\beta c)^4} \left[\frac{2\alpha^2 - \alpha x_f - 3x_f^2}{2\alpha^3 x_f(\alpha + x_f)} - \frac{2}{\alpha^3} \ln\left(\frac{\alpha + x_f}{2x_f}\right)\right] \tag{4.26}$$

Substituting equation (4.26) in yields an expression:

$$\langle u'_{R,sy}\rangle = \frac{4\Gamma^6 \nu F_\nu(sy) d_L^2 \tau R_{cl}^2}{3(R_m - R_b)} \left(\frac{4}{(\beta c)^4} \left[\frac{2\alpha^2 - \alpha x_f - 3x_f^2}{2\alpha^3 x_f(\alpha + x_f)} - \frac{2}{\alpha^3} \ln\left(\frac{\alpha + x_f}{2x_f}\right)\right]\right) \tag{4.27}$$

Equation (4.27) is given in the limit $x_f \ll \alpha$, further simplification yields:

$$\langle u'_{R,sy}\rangle = \frac{4\Gamma^6 \nu F_\nu(sy) d_L^2 \tau R_{cl}^2}{3(R_m - R_b)} \left(\frac{4}{(\beta c)^4} \left[\frac{1}{\alpha^2 x_f} + \frac{2}{\alpha^3} \ln\left(\frac{t_f}{2x_f}\right)\right]\right) \tag{4.28}$$

To calculate the value of $\langle u'_{R,sy}(t_1)\rangle$, assume that $\beta \approx 1$, and a few other parameters first need to be calculated. The actual value of α can be determined, which is dependent on R_m, given by: $R_m = 2\Gamma^2 c\Delta t$. With $\Delta t = 11\ days = 950400\ s\ t_{11}$ and $\Gamma = 10\ \Gamma_1$, this yields:

$$R_m = 5.7 \times 10^{18}\ cm\ \Gamma_1^2 t_{11} \tag{4.29}$$

R_b also needs to be calculated. Using the variability timescale constraint

$$R_b \leq 10^{15} \frac{\left(\frac{t_{var}}{hr}\right)\left(\frac{\delta}{10}\right)}{(1+z)} cm \tag{4.30}$$

Data from Hayashida et al. [2015] indicate a characteristic variability time scale for 3C 279 $t_{var} \approx 2\ days = 48\ hr$ and the redshift is, $z = 0.536$. From $\theta = \frac{1}{\Gamma}$ the Doppler factor is $\delta = \Gamma = 10$. This yields a blob size of:

$$R_b = 3.1 \times 10^{16}\ cm\ \frac{t_{var}}{2\ days}\ \frac{\delta}{10} \tag{4.31}$$

Using R_m and R_b to calculate the values of $\alpha = 1.9 \times 10^8\ s\ t_{11}\Gamma_1^2$, and t_f:

$$t_f = \frac{5.7 \times 10^{18}\ cm\ \Gamma_1^2 t_{11}\ -\ 6.3 \times 10^{16}\ cm}{3 \times 10^{10}\ cm.s^{-1}} = 1.9 \times 10^8\ s\ t_{11}\Gamma_1^2\ \approx \alpha \tag{4.32}$$

Using the above results of t_f and α it is found that $x_f = 2 \times 10^6\ s\ R_{16}$

Substituting in the values of: $\nu F_\nu = 2 \times 10^{-11}\ erg \cdot cm^{-2} \cdot s^{-1}$, $d_L = 10^{28}\ cm$, $R_{cl} = 5 \times 10^{15}\ cm\ R_{15}$, t_f, x_f, α, and $\tau = 0.001\ \tau_{-3}$, chosen as 0.1 because only a small fraction of the photons are reflected back into the still emitting jet, into equation (4.27), the energy density yields:

$$\langle u'_{R,sy}\rangle = 35.2\ erg \cdot cm^{-3}\ t_{11}^{-3}\tau_{-3}R_{15}R_{16}^{-1} \tag{4.33}$$

To find the photon number density, use the observed synchrotron photon energy, $E = 10^{-12} erg \approx 1eV$:

$$n_{ph} = \frac{\langle u'_{R,sy}\rangle}{E'_{sy}} = \frac{\langle u'_{R,sy}\rangle}{\Gamma E_{sy}} = 3 \times 10^{12}\ cm^{-3}\ t_{11}^{-4}\tau_{-3}R_{15}^2\Gamma_1^{-1} \tag{4.34}$$

4.1.2 Density calculation from energy loss rates

In this section, the target photon number density for $p\gamma$-interactions needed to produce a radiative output comparable to the proton-synchrotron GeV γ-ray flux, is calculated. Firstly the Lorentz factor of relativistic protons which produces the peak of the Fermi-LAT GeV spectrum needs to be found. This can be calculated from the synchrotron frequency:

$$\nu_{sy} = 4.2 \times 10^6\ \delta B_G \gamma_p^2 Z \frac{m_e}{m_p} Hz \tag{4.35}$$

Let Z = 1 and from the data, we see that $\nu_{sy} = 10^{25} Hz$, then γ_p is:

$$10^{25} Hz = 4.2 \times 10^6 (1836)^{-1} \gamma_p^2 B_G \delta Hz \tag{4.36}$$

$$\gamma_p = 2.5 \times 10^9 B_G^{-\frac{1}{2}} \delta^{-\frac{1}{2}} \tag{4.37}$$

The synchrotron cooling rate is taken from Böttcher et al. [2013]:

$$\dot{\gamma}_{p,sy} = -\frac{c\sigma_T B^2}{6\pi m_e c^2} \left(\frac{m_e}{m_p}\right)^3 \gamma_p^2 \tag{4.38}$$

where $\sigma_T = 6.65 \times 10^{-25} cm^2$ is the Thomson cross-section, the mass ratio is $\left(\frac{m_e}{m_p}\right) = 1836^{-1}$, and the value of $\dot{\gamma}_{p,sy}$ is:

$$\dot{\gamma}_{p,sy} = -6.4 \times 10^3 \ B_G \delta^{-1} s^{-1} \tag{4.39}$$

The photon-pion energy loss-rates are approximated as:

$$\dot{\gamma}_{p,p\gamma} = -c\langle\sigma_{p\gamma} f\rangle n_{ph}(\epsilon^*)\epsilon^* \gamma_p \tag{4.40}$$

Where the $p\gamma$ interaction cross section is given by $\langle\sigma_{p\gamma} f\rangle \approx 10^{-28} \ cm^2$ and $\epsilon^* \approx 10^{-6}$ is the energy of target photons interacting with protons at energy E at the delta resonance. The proton synchrotron and p-gamma radiative outputs are similar, if $\dot{\gamma}_{p,sy} = \dot{\gamma}_{p,p\gamma}$, then:

$$n_{ph}(\epsilon^*) = \frac{\sigma_T B^2}{6\pi \langle\sigma_{p\gamma} f\rangle m_e c^2} \left(\frac{m_e}{m_p}\right)^3 \frac{\gamma_p}{\epsilon^*} cm^{-3} \tag{4.41}$$

Substitute the variables in to find the resulting density of the photons:

$$n_{ph}(\epsilon^*) = 3.4 \times 10^{14} \ B_G^{\frac{3}{2}} \delta^{\frac{1}{2}} cm^{-3} \tag{4.42}$$

The energy density can be calculated from:

$$n_{ph}(\epsilon^*)\epsilon^* = \frac{u'_{ph}}{m_e c^2} \tag{4.43}$$

This yields:

$$u'_{ph} = 2.8 \times 10^2 \ B_G^{\frac{3}{2}} \delta^{-\frac{1}{2}} \ erg.cm^{-3} \tag{4.44}$$

This is one order of magnitude larger than the result in equation (4.33), therefore, given appropriate parameters, the result can be of the same order of magnitude. In case of a larger cloud, $R_{cl} > 5 \times 10^{15} \ cm \ R_{cl,17}$, or a smaller emission region or even a larger reflective fraction of the cloud, τ, the target photon density will be increased. Consequently, analytically the Hadronic Synchrotron Mirror Model is quite plausible. Clouds acting as mirrors are found in the broad line region (BLR) crossing the path of the jet and can be detected studying the emission lines of the AGN [Dar and Laor, 1997]. Seed photons are needed for

a dense enough target photon field to actually exist for the jet to interact with. That supports the case of having external photon fields for the jet to interact with. The mirror in our model might be a BLR cloud.

Chapter 5

Program

5.1 Outline

The previous chapter focussed on the analytical calculations, in this chapter the numerical calculations will be discussed. The idea behind the code is to use the electron synchrotron photon emission and to evaluate how long it takes to hit the cloud and then be reflected back into the still emitting jet as illustrated in figure 4.2. The program was split into different routines and thus pieces of code, as described roughly in the list below.

- Get the parameters describing the relativistic proton population from a proton synchrotron fit to the Fermi-LAT gamma-ray spectrum.
- Numerical evaluation of the target photon field as a function of time.
- Pion production and pion-decay products.
- Calculate the $\gamma\gamma$-opacity.
- Calculate the resulting electromagnetic cascades to find the emerging SED.

5.2 Proton spectrum

For the numerical evaluation of the hadronic synchrotron mirror model, we need to determine the relevant system parameters. We need to find the normalisation and the spectral break of the proton spectrum from the proton synchrotron component to use in the next step of the program. B-fields of $10\ G$ are usually required in plausible hadronic models for blazars. In order to determine the parameters of the relativistic proton population, we fit the Fermi-LAT gamma-ray spectrum with a proton synchrotron radiation spectrum. We first tried to model the data with a power-law and then used a broken power-law.

5.2.1 Power-law

We are trying to model the Fermi-LAT data of the spectral energy distribution of the flare. We use a simple power-law approach:

$$N_p(\gamma_p) = N_0 \gamma_p^{-p} \tag{5.1}$$

where γ_p is the proton Lorentz factor covering the following range where: $1 < \gamma_p < \gamma_{max} = 10^{10}$, γ_{max} is the Lorentz factor that corresponds approximately to the maximum energy these particles can accelerate to, ie. $E_{max} = 10^{19} eV$. The synchrotron-radiation spectral index is given by $\alpha = \frac{p-1}{2}$, which is the negative slope of a log $F_\nu(\nu)$ - log ν plot, from which the particle distribution index, p, can be found. Equation (4.37) represents the proton Lorentz factor where radiative losses become more dominant than adiabatic losses.

In order to model the spectrum, we use an approximation based on the asymptotic behaviour of the single-particle synchrotron emissivity [Böttcher et al., 2012]. We calculate the frequency differentiated luminosity:

$$L_{\nu'}^{'} = \frac{32\pi c}{9\Gamma^{\frac{4}{3}}} \left(\frac{e^2}{m_p c^2}\right)^2 \frac{B^2}{8\pi} N_0 \nu^{\frac{1}{3}} \int_1^{\gamma_{max}} \gamma_p^{2-p} \frac{e^{-\frac{\nu'}{\nu_c(\gamma_p)}}}{\nu_c^{\frac{4}{3}}} d\gamma_p \tag{5.2}$$

where $\nu_c = 2.3 \times 10^3 \gamma_p^2 \; B_G \; Hz$. The flux is then given by:

$$\nu F_\nu^{obs} = \frac{\delta^4 \nu' L_\nu^{'}}{4\pi d_L^2 (1+z)} \tag{5.3}$$

where $\nu = \nu' \frac{\delta}{(1+z)}$ for conversion from emission to observer's frame.

Considering the broadband SED of 3C279 in Figure 4.1, the extrapolation of the power-law proton synchrotron spectrum to lower X-ray frequencies would greatly overshoot the X-ray data in Fig 2.1 where the blazar sequence which applies to 3C 279 is shown.

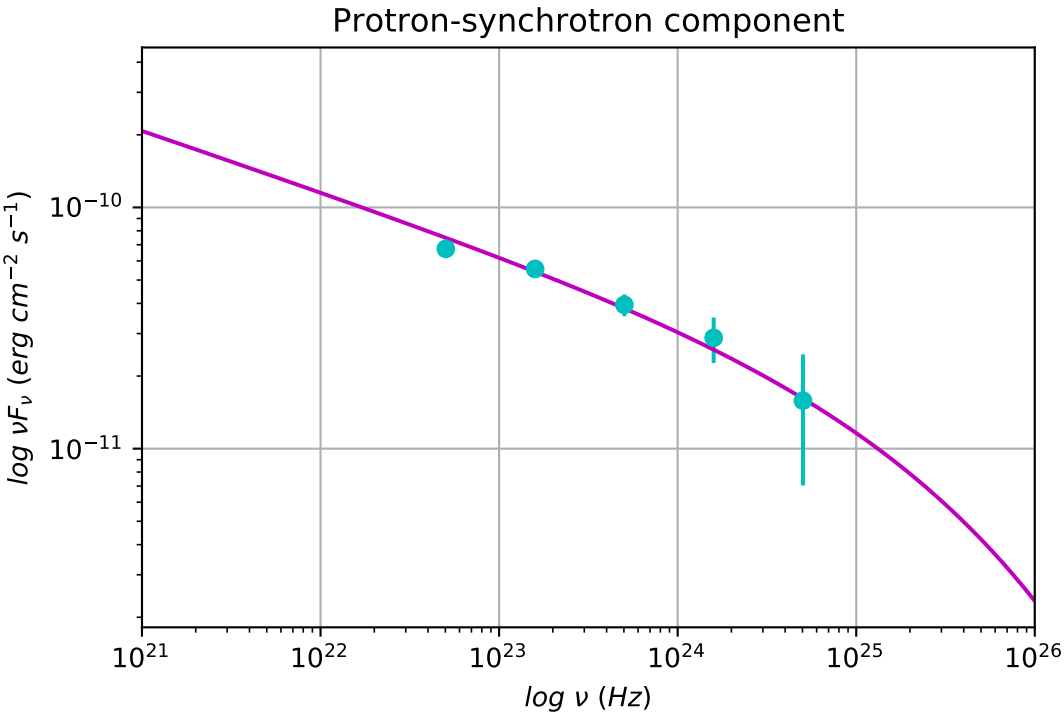

Figure 5.1: The Fermi-LAT data points modeled by a power-law representation of the proton distribution, with the data points in cyan and the power-law in magenta

To rectify this situation, we used a broken power-law with an exponential cut-off instead.

5.2.2 Broken power-law

The broken powerlaw is represented by the equation:

$$N_p(\gamma_p) = N_0 \left(\frac{\gamma_p}{\gamma_b}\right)^{-p_{1,2}} e^{-\frac{\gamma_p}{\gamma_c}} \tag{5.4}$$

To get the correct spectral shape a slope of $p_1 = 1.5$ was estimated for $\gamma_p < \gamma_b$ and a slope was approximated to the Fermi data for $\gamma_p > \gamma_b$ with $p_2 = 3.5$.

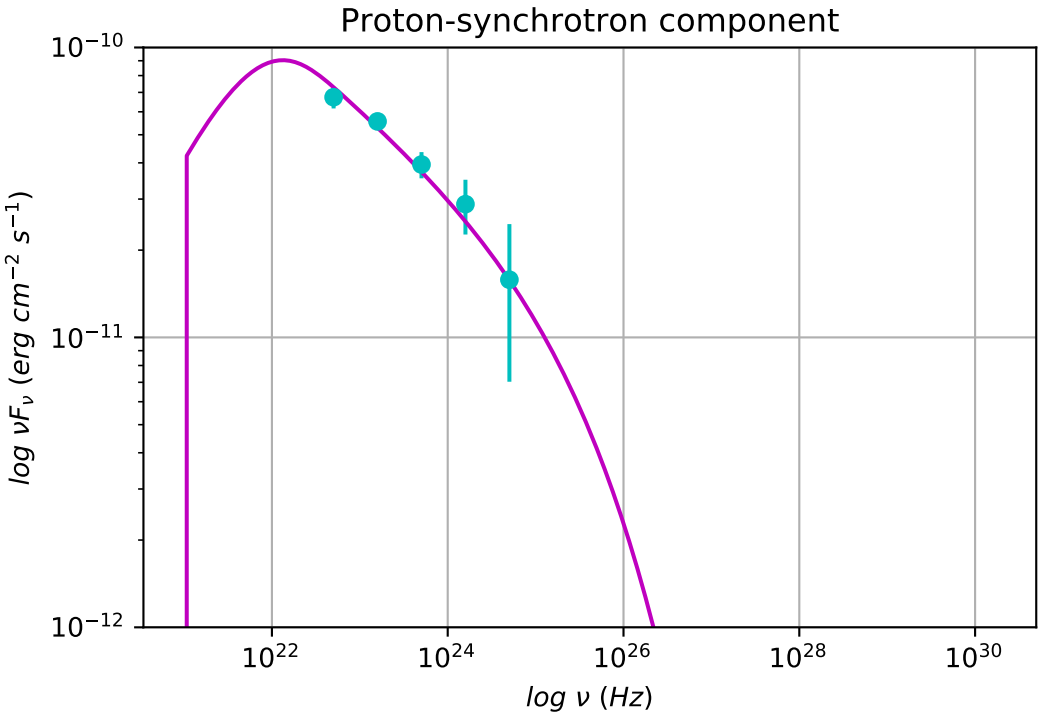

Figure 5.2: The best fit of the broken power-law with exponential cut-off (in magenta) to the Fermi-LAT data (in cyan).

To get the fit in Figure 5.2, a "fit-by-eye" method is used by using plausible values for parameters not constrained by observations while other parameters are adjusted. The Doppler factor, δ, was set to $\delta = 10$ and kept fixed as well as the Bulk Lorentz factor $\Gamma = 10$. The normalisation (N_0) and magnetic field (B) were varied. The fit in Fig. 5.2 was produced by $B = 100\ G$ and $N_0 = 2.5 \times 10^{37}$. Equally good fits for different values of B, can be found if N_0 and γ_b are varied accordingly. A list of all the prameters used in the proton-synchrotron fit is given in Table 5.1.

N_0	2.5×10^{37}
B	$100\ G$
γ_b	9.8×10^7
γ_c	6.6×10^9
δ	10

Table 5.1: A list of the parameters used for the proton-synchrotron fit.

γ_c is the high-energy cut-off of the proton spectrum, which was predeter-

mined using:

$$\gamma_c = \sqrt{\frac{\nu_{crit}}{\nu_0}} \tag{5.5}$$

where ν_0 is the frequency normalisation, such that $\nu_{sy} = \nu_0 \gamma_p^2$:

$$\nu_0 = 2.3 \times 10^3 B \frac{\delta}{(1+z)} \tag{5.6}$$

and $\nu_{crit} = 6 \times 10^{24}\ Hz$. γ_b is the Lorentz factor where the power-law is broken and is given by:

$$\gamma_b = \sqrt{\frac{\nu_b}{\nu_0}} \tag{5.7}$$

with $\nu_b = 1.5 \times 10^{21}\ Hz$, which is found by postulating a spectral break at a frequency just below the Fermi-LAT band. The degeneracy between the magnetic field, Doppler factor and the proton Lorentz factors can be seen when looking at the synchrotron frequency:

$$\nu_{sy} = 4.2 \times 10^6 \frac{m_e}{m_p} \gamma_p^2 B \frac{\delta}{(1+z)} \tag{5.8}$$

To get rid of degeneracies, some independent methods to determine the bulk Lorentz factor and the Doppler factor, can be investigated. The following parameters were found to fit the Fermi-LAT data well: $N_0 = 2.5 \times 10^{37}$, $\gamma_b = 9.8 \times 10^7$ and $\gamma_c = 6.6 \times 10^9$, using $B = 100\ G$.

5.3 Numerical evaluation of the target photon field

The electron-synchrotron component was used to calculate the target photon field. The assumption is that there are both protons and electrons in the jet. We use known values from the quiescent state of the jet during the study in Böttcher et al. [2013] to calculate the target photon spectrum. The photons and protons interact to produce pions which then decay, producing secondary pairs and photons.

The analytical calculations from Section 4.1 (Equation 4.1 - 4.17) are reproduced numerically for the first part of the mirror model calculation. This documents the target photon energy density at every timestep as well as the distance from the source to the mirror at every timestep and saves the values in seperate arrays.

While the blob is still moving toward the mirror and the photons are being reflected back, the density is growing and as soon as all the reflected photons have moved through the blob, the density decreases to zero. The synchrotron target photon density is found by combining equations (4.15) and (4.16) :

$$\Delta u_{sy} = \frac{\Gamma^3 F(t) A \Delta t}{V} \tag{5.9}$$

$F(t)$ is the flux from the reflected electron-synchrotron emission and is evaluated by equation (4.14). This is denoted by an if statement in the code where Eq. (5.9) denotes the contribution Δu_{sy} that is added for photons newly arriving from the mirror at the "top" of the emission region at time t_3 and subtracted when photons arrive at the "bottom" of the emission region at time t_4 when the reflected photons move completely through the emission region. The synchrotron photon energy density is used to calculate the normalisation for the photon number spectrum:

$$n_0 = \frac{u_{sy}(1-\alpha)}{m_e c^2(\epsilon_2^{1-\alpha} - \epsilon_1^{1-\alpha})} \tag{5.10}$$

From this, we can generate the target photon spectrum for photo-pion production at every time step, as shown in Figure 5.3:

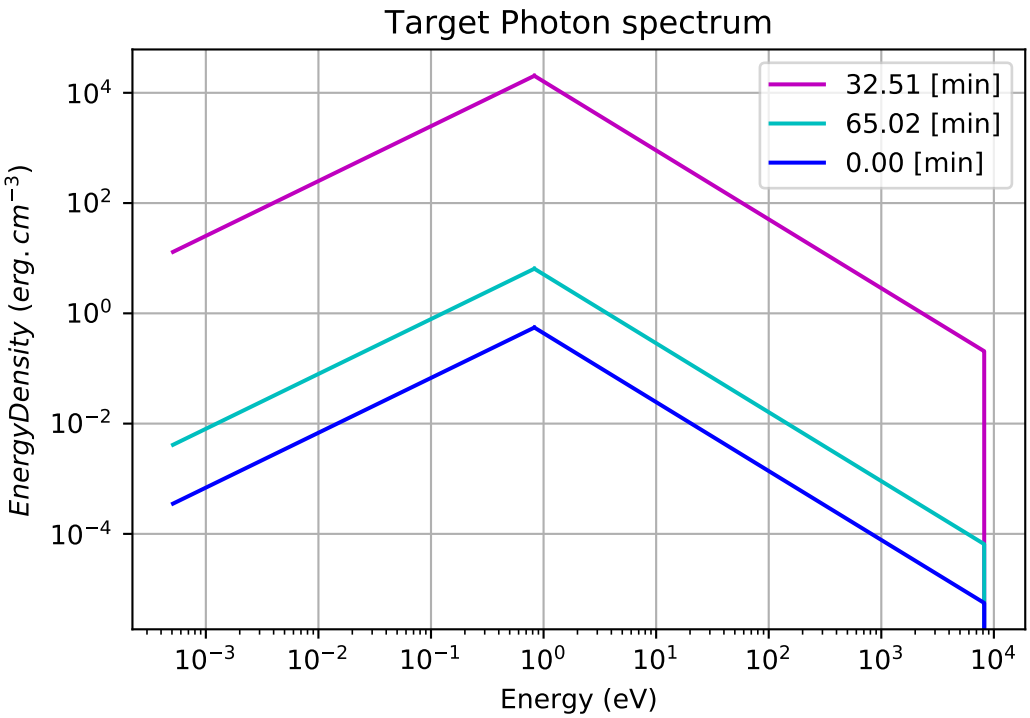

Figure 5.3: The target photon spectrum at certain times since the onset of the orphan flare. We can see the energy density shoot up after some time passes and then come down again after more time passes.

The shape of the target photon spectrum is due to a break in the electron spectrum. Using Figure 4.1 as a guide for the energy range needed, ϵ_1 and ϵ_2 are the dimensionless energies calculated from the frequencies read from Figure 4.1 as $\nu_1 = 10^{13}\ Hz$ and $\nu_2 = 10^{17}\ Hz$. The different lines in Figure 5.3 shows how the energy density shoots up as the reflected photons are enetring the still emitting jet and how it goes back down after the emission region passes through the cloud.

5.4 Pion-decay products

The photon and positron number spectra are calculated through the decay of pions from equations (5.12) and (5.13) in Böttcher and Dermer [1998]. To get to these number spectra, the photo-pion differential cross-section is needed, we use $\sigma_0 = 2 \times 10^{-28}\ cm^2$ and $E_\Delta = 330 MeV$ to find it. The pions are produced near threshold energy in the proton's rest frame. The p-gamma cross section is approximated by a Heaviside function around the Delta resonance energy and the following equation for the photon spectrum from photo-pion decay, where the energy of the neutral pion is split into two halves carried by two photons, can be found:

$$\dot{N_\gamma^{\pi_0}}(\epsilon) = \sigma_0 n_0 \frac{c N_0 E_\Delta}{2 m_\pi c^2 (\alpha + 1)} \times \tag{5.11}$$

$$\int_{max[\epsilon \frac{m_e}{m_\pi}, \gamma_b, \frac{E_\Delta}{2\epsilon_2 m_e c^2}]}^{\gamma_{cr,max}} d\gamma_\pi \gamma_\pi^{-(2+s)} \left(max \left[\epsilon_1, \frac{E_\Delta}{2\gamma_\pi m_e c^2} \right] - \epsilon_2^{-(\alpha+1)} \right) \tag{5.12}$$

where γ_b represents the minimum Lorentz factor beyond which we have the power-law proton spectrum. The rate of positron production from charged-pion decay can be approximated to be:

$$\dot{N_{e^+}}(\gamma_+) = \dot{N_\gamma^{\pi_0}}(\epsilon = 2\gamma_+) \tag{5.13}$$

We assume that the charged pions are produced by the same rate as the neutral pions and after decaying only a quarter of the energy goes to the positron as three neutrinos are also produced. An example of the π^0 photon production rate spectrum is shown in Figure 5.4:

and an example of the positron production spectrum for the same time step is shown in Figure 5.5:

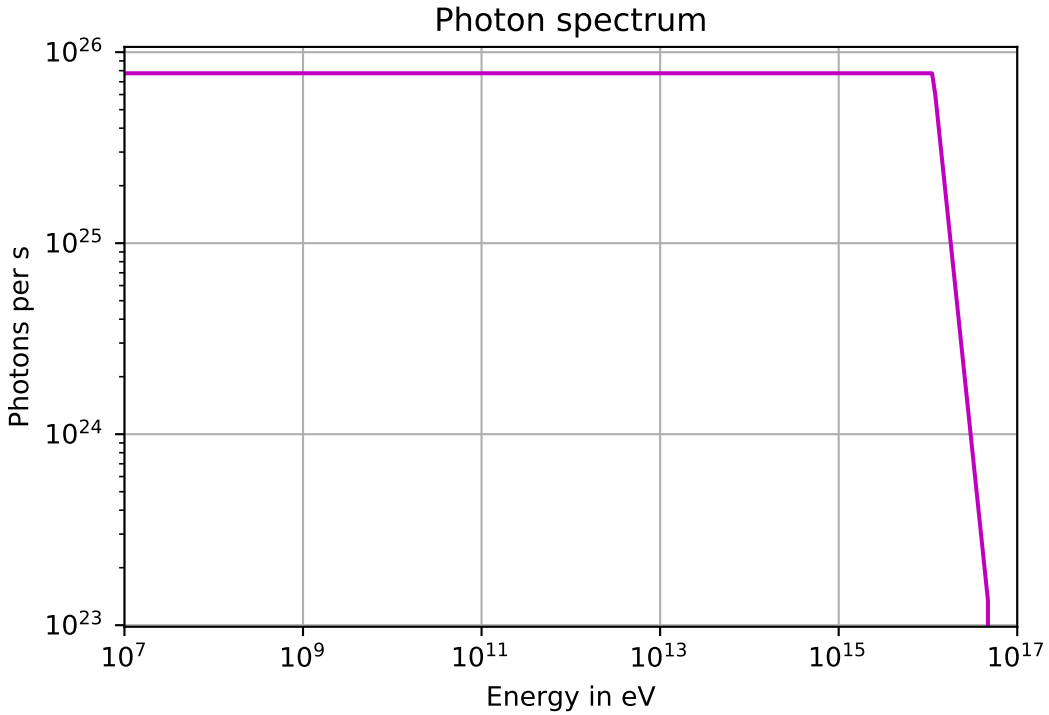

Figure 5.4: The photon spectrum produced from the π^0-decay, 75 min after the onset of the flare.

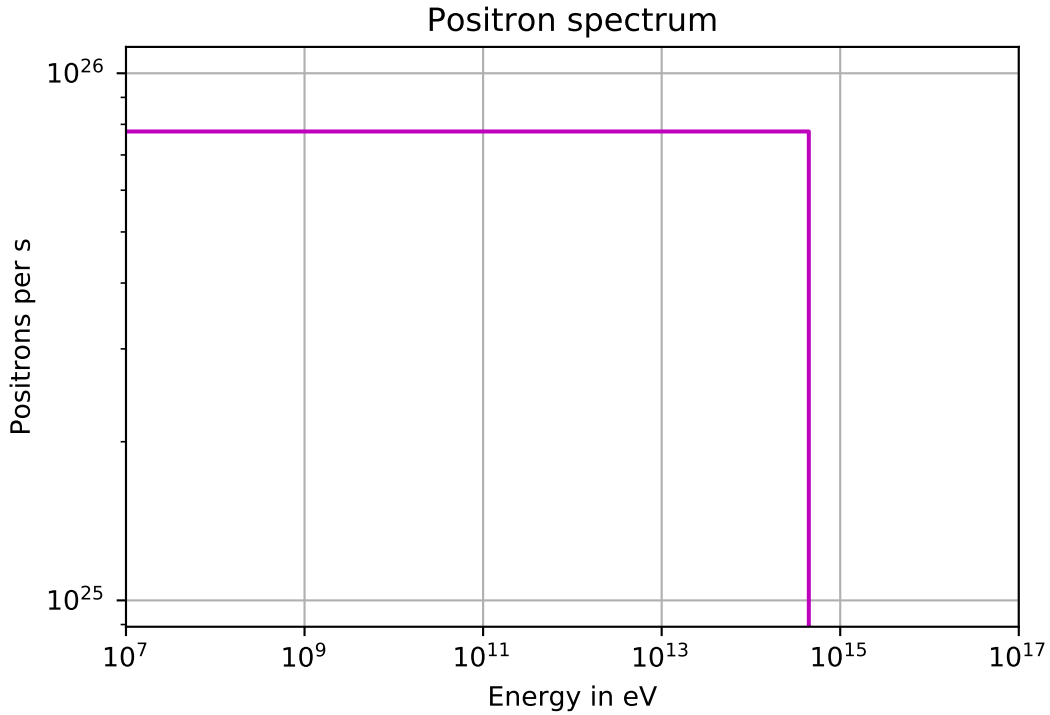

Figure 5.5: The positron spectrum produced from the π^+-decay, 75 min after the onset of the flare.

5.5 The $\gamma\gamma$-opacity

Photons from the photo-pion decay processes emerge in the ultra-high-energy (UHE) regime. The UHE regime is very opaque for $\gamma\gamma$ absorption. A synchrotron component in the IR/optical/UV range will be needed to produce absorption for GeV- TeV photons. $\tau_{\gamma\gamma}$ is the $\gamma\gamma$-opacity, which means it is the fraction of particles that get absorbed by $\gamma\gamma$ interactions taking place when $\tau_{\gamma\gamma} \ll 1$ and the rest of the time the fraction that gets absorbed is e^{τ}, which initiate pair cascades. This can be pre-calculated. Looking at the observed electron-synchrotron component, a target photon spectrum and normalisation is identified, between the frequencies of 10^{13} and 10^{17} Hz. To calculate the $\gamma\gamma$-opacity, we need to consider the $\gamma\gamma$-cross-section in the delta-function approximation:

$$\sigma_{\gamma\gamma}(\epsilon_\gamma) \approx \frac{\sigma_T}{3}\epsilon_t \delta\left(\epsilon_t - \frac{2}{\epsilon_\gamma}\right) \tag{5.14}$$

Integration of $\sigma_{\gamma\gamma}$ and the synchrotron photon spectrum gives us the $\gamma\gamma$-absorption:

$$\tau_{\gamma\gamma}(\epsilon_\gamma) \approx R \int \sigma_{\gamma\gamma} n_t(\epsilon_t)\ d\epsilon_t \tag{5.15}$$

$$\tau_{\gamma\gamma}(\epsilon_\gamma) \approx \frac{R\sigma_T}{3}\frac{2}{\epsilon_\gamma} n_t\left(\frac{2}{\epsilon_\gamma}\right) \tag{5.16}$$

where the synchrotron photon spectrum is approximated as a simple power-law between the above-mentioned frequencies:

$$n_t\left(\frac{2}{\epsilon_\gamma}\right) = n_0\left(\frac{2}{\epsilon_\gamma}\right)^{-(1+\alpha)} \tag{5.17}$$

Substituting Eq. (5.17) into Eq. (5.16), leads to:

$$\tau_{\gamma\gamma} = \frac{2^{-\alpha}\sigma_T R_b n_0 \epsilon_\gamma^{\alpha}}{3} \tag{5.18}$$

with $\alpha = 1.25$. n_0 is the normalisation of the photon spectrum, which can be calculated by considering the density of the target photon spectrum:

$$u = \frac{L}{4\pi R^2 c} \tag{5.19}$$

Rearranging that equation leaves us with:

$$L_\epsilon = 4\pi R_b^2 c u_\epsilon \tag{5.20}$$

With the energy density given as:

$$u_\epsilon = n(\epsilon) m_e c^2 \epsilon \tag{5.21}$$

And:

$$n(\epsilon) = n_0 \epsilon^{-(1+\alpha)} \tag{5.22}$$

This leads to:

$$L_\epsilon = 4\pi R_b^2 c m_e c^2 n_0 \epsilon^{-\alpha} \tag{5.23}$$

It is well known that the flux is given by:

$$\nu F_\nu = \epsilon F_\epsilon = \frac{\epsilon^{'} L_{\epsilon'}}{4\pi d_L^2} \frac{\delta^{4+\alpha}}{(1+z)} \tag{5.24}$$

Which leads to:

$$\epsilon F_\epsilon = \frac{R_b^2 m_e c^3 n_0 \epsilon^{1-\alpha} \delta^{4+\alpha}}{d_L^2 (1+z)} \tag{5.25}$$

Rearranging this yields:

$$n_0 = \frac{\epsilon F_\epsilon d_L^2 (1+z)}{R_b^2 m_e c^3 \epsilon^{1-\alpha} \delta^{4+\alpha}} \tag{5.26}$$

where, $\nu F_\nu = \epsilon F_\epsilon = 2 \times 10^{-11}\ erg.cm^{-2}.s^{-1}$ is the Fermi-LAT observed peak of the electron-synchrotron spectrum from the primary flare, $d_L = 10^{28}\ cm$, $R_b = 6.3 \times 10^{16}\ cm$, $\delta = 10$, using $\epsilon = 10^{-6}$. This yielded a normalisation of $n_0 = 5.6\ cm^{-3}$. Thus $\tau_{\gamma\gamma} = 3.35 \times 10^{-7} \epsilon_\gamma^{-\alpha}$. The emission region becomes optically thick, $\tau_{\gamma\gamma} = 1$, to $\gamma\gamma$-absorption at $\epsilon_1 = 6.6 \times 10^6$, about 3 TeV.

5.6 Cascade program

The photons from the π^0-decay products are injected at high energies into the jet and form pair cascades. The injected power is then reprocessed to lower energies through $\gamma\gamma$-pair production and electron-positron pair production, [Böttcher et al., 2012]. The production spectra for the photons are needed. Using a semi-analytical approach, the injection rates are known from the spectra result from numerical calculations as shown in equations (5.12) and (5.13), which are integrated over the γ_π energy grid starting from the highest photon energies moving to the lower energies to obtain production spectra. $\gamma\gamma$-absorption takes place, as mentioned in section 2.3, and the optical depth $\tau_{\gamma\gamma}$ is precalculated. The spectrum of the observable escaping photons can be calculated:

$$\dot{N}_\epsilon^{esc} = \dot{N}_\epsilon^{em} \left(\frac{1 - e^{-\tau_{\gamma\gamma}[\epsilon]}}{\tau_{\gamma\gamma}[\epsilon]} \right) \tag{5.27}$$

where $\dot{N_{\epsilon}^{em}} = \dot{N_\epsilon^0} + \dot{N_\epsilon^{sy}}$, with contributions from the high-energy, first-generation γ-rays ($\dot{N_\epsilon^0}$) and the synchrotron emission from the pairs in the cascade. Pair cascades produced by UHE γ-rays are thus very important for hadronic modeling and need to be included. Following the calculations done in Böttcher et al. [2013] an implicit solution is found:

$$N_e(\gamma) = \frac{1}{\nu_0 \gamma^2} \int_{\gamma}^{\infty} d\tilde{\gamma} \left\{ Q_e(\tilde{\gamma}) + \dot{N}_e^{\gamma\gamma}(\tilde{\gamma}) - \frac{N_e(\tilde{\gamma})}{t_{esc}} \right\} \tag{5.28}$$

where $Q_e(\gamma)$ represents the injection rate of the pairs, $\dot{N}_\epsilon^{\gamma\gamma}(\gamma)$ is the pair production rate and t_{esc} is the escape timescale. Particles need to be injected at the highest energies so that $Q_0(\gamma) \neq 0$ and $\dot{N}_\epsilon^0 \neq 0$ and the solution at the highest γ's can be used to calculate the values at lower energies. We employ a code written by Professor Markus Böttcher and used in Böttcher et al. [2013]. The output from the cascade code was calculated in the co-moving frame of the emission region, to convert it to the observer's frame and get the actual logarithmic flux, a factor of $\frac{m_e c^2 \delta^4}{4\pi d_L^2 (1+z)}$ needs to be added to νF_ν and a factor of $\frac{\delta}{(1+z)}$ to the frequency.

Chapter 6

Results

The results for the application of the hadronic synchrotron mirror model to 3C 279's 28 January 2018 orphan flare are displayed in this chapter. A condition for the model to work was that there should be a dense enough target photon field for photo-pion production to take place. Figure 6.1 reveals that as the photons are reflected back into the jet, there is a steep increase in the photon density. As seen from the calculations in Chapter 4.1.1 and 4.1.2, there is a dense enough target photon field. We thus employ the code described in Chapter 5 to fit the orphan VHE gamma-ray flare observed by H.E.S.S. in Figure 2.4. The relevant parameters that were used in this study are:

- $R_{cl} = 5 \times 10^{15}$ cm - For our analytical estimates, we scaled the radius of the cloud as $R_{cl} = 10^{17}$, but it seemed that our model was too effective at boosting the photon-pion production as well as the Fermi-Lat, that should not be boosted, so we reduced it.
- $\tau = 0.001$ - The fraction of photons that are reflected back into the emitting cloud, we reduced this from $\tau = 0.1$ to fit the smaller cloud size.
- $\delta = 10$ - The doppler factor was chosen and kept constant through the parameter study.
- $N_0 = 2.5 \times 10^{37}$ - The normalisation was the parameter that was varied the most to find the perfect fit of the proton-synchrotron spectrum from the quiescent state. The other parameters were fixed before the normalisation.
- $\gamma_b = 9.8 \times 10^7$ - The Lorentz factor that signifies the break in the proton spectrum, this was calculated using the Fermi-LAT peak as well as the critical frequency that is dependant on the magnetic field.
- $B = 100$ G - The Magnetic field needs to be quite high to accelerate protons to these relativistic energies. This parameter was also varied quite a bit and it seemed to fit the data the best when it was set to the maximum number that would still make sense realistically.

All the parameters mentioned in this list above were changed with respect to the values used for the analytical estimates. The target photon field density over time is displayed in Figure 6.1.

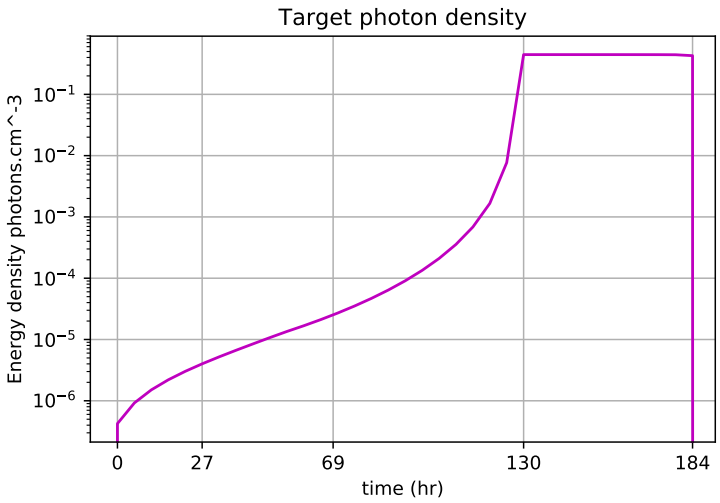

Figure 6.1: The target photon density against the time in the AGN rest frame in hours as the orphan flare is taking place.

time = 0 hr denotes the start of the flare when the density is > 0 and time = 184 hr is the time at which the reflected synchrotron photons pass.

The total gamma-ray SED, along with the individual proton-synchrotron and photo-pion production components of the flare are shown in Figures 6.2 and 6.3:

The spectral energy distribution is obtained by photo-pion-induced cascade emission with contributions from proton-synchrotron radiation. The cascade component requires a very large jet power to produce a VHE flux as measured during the orphan flare. Hadronic jet models typically require jet powers of the order $L_p \sim 10^{47} - 10^{49}$ erg.s^{-1} [Böttcher et al., 2013]. The jet power for this flare was estimated as, for the proton spectrum:

$$L_p \sim \pi R_b^2 c \Gamma^2 \gamma_b^2 m_p c^2 \frac{N_0}{V_b} \sim 2.1 \times 10^{47} \text{ erg.s}^{-1} \tag{6.1}$$

where $V_b = \frac{4}{3}\pi R_b^2$. To see if the jet is proton dominated or Poynting flux dominated we need to calculate the jet power in terms of the magnetic field:

$$L_B \sim \pi R_b^2 c \Gamma^2 \frac{B^2}{(8\pi)} \sim 9.4 \times 10^{46} \text{ erg.s}^{-1} \tag{6.2}$$

The jet power seems to be close to equipartition, with a slight dominance of the power in protons. The Eddington luminosity for 3C 279 is at most $L_{Edd} =$

1.3×10^{47} erg.s^{-1}, because 3C 279 has a BH mass of $(3-8) \times 10^8$ M$_\circ$. In follow-up work the parameters can be tweaked to find if there is a parameter set that leaves the jet power below that of the Eddington luminosity but is sufficient to produce the orphan flare. Figure 6.3 displays the Fermi-LAT flux, which for the highest points is significantly affected, but for the low-energy bins, the Fermi-LAT flux is not significantly affected by the addition of the photo-pion contribution during the VHE flare. This accurately represents the orphan flare. The photo-pion component can be seen becoming more prominent where the reflected photons reach the top of the emission region. Figure 6.4 displays the lightcurves of 3C 279, at three different gamma-ray energies, with the expected behaviour of a spike in flux at the time when the photons get reflected back into the jet. The VHE flare is represented by the model flux at 100 GeV. There is a flare of a factor of ~ 2 in flux at 1 GeV. Thus, the total Fermi-LAT photon flux, dominated by the photon number at the lowest energies, is expected to exhibit only a minor flare, compared to the giant (factor > 10) VHE gamma-ray flare. The observed time differs from the time in the AGN rest frame, because of light-travel-time effects. The light-travel-time effect leads to a contraction of the observed time as $t_{obs} = \frac{t_{AGN}}{\Gamma^2}$. The model predicts a significant flare of about 30 min duration.

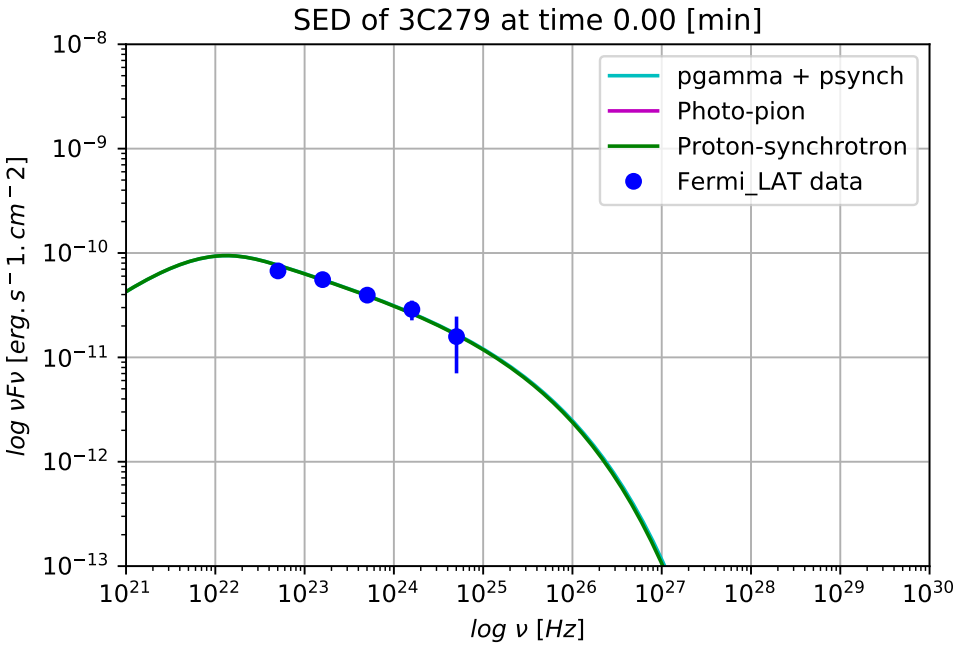

(a)

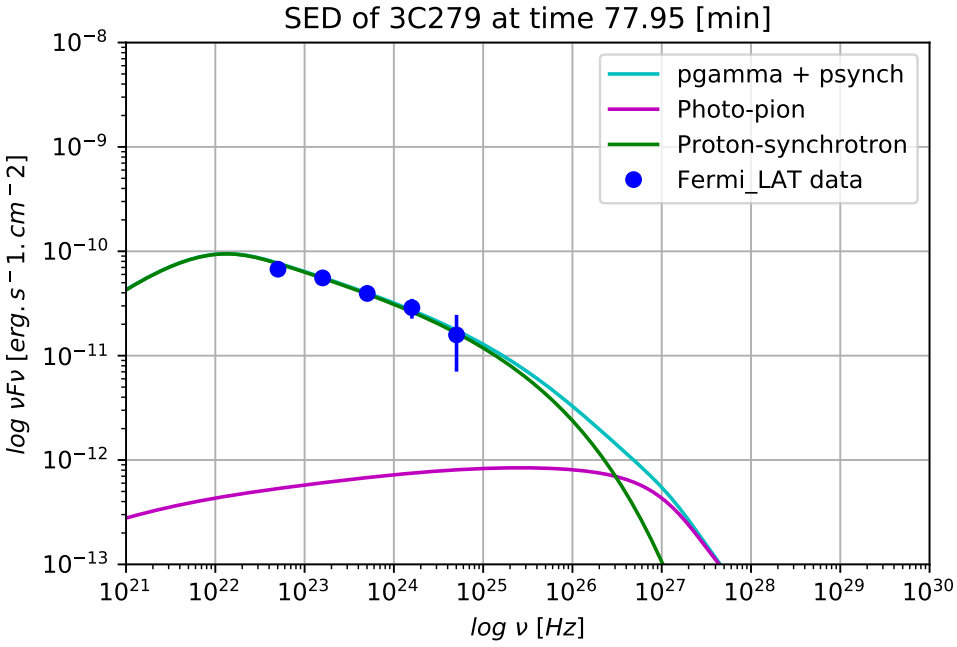

(b)

Figure 6.2: The SED of 3C279 produced by the pair cascades of the VHE γ-rays from the photo-pion interactions (pink line) and the proton-synchrotron component (green line), the sum of the two components (cyan line). (a) happens at $t = 0$ min, right as the energy density is non-zero and (b) takes place $t = 78$ minafter the flare started, and the Fermi-LAT data points are plotted for reference (blue dots).

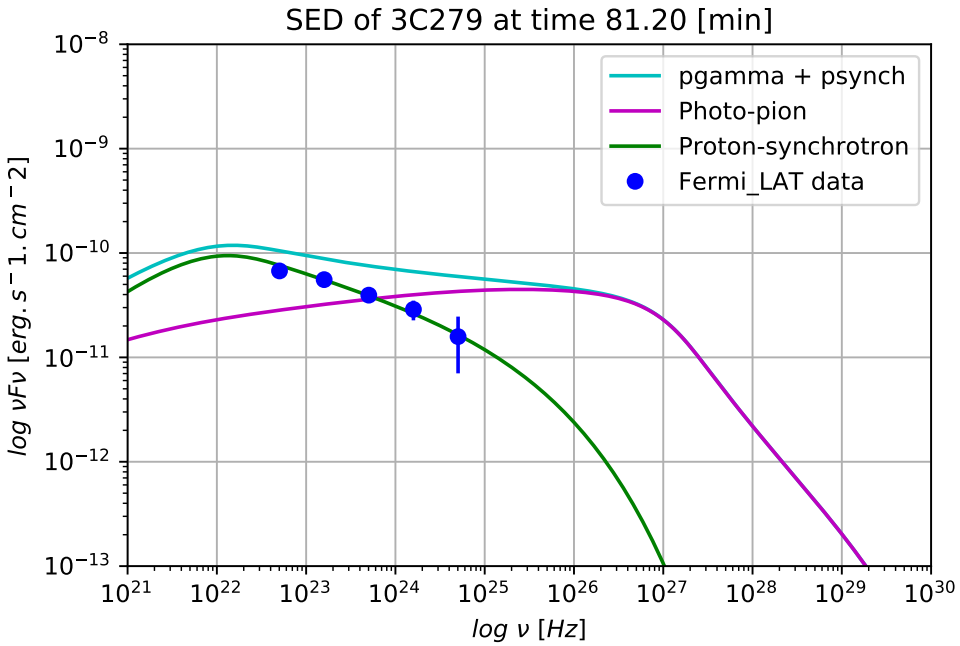

Figure 6.3: The SED of 3C279 produced by the pair cascades of the VHE γ-rays from the photo-pion interactions (pink line) and the proton-synchrotron component (green line), the sum of the two components (cyan line) at 81.25 min after the flare started, and the Fermi-LAT data points are plotted for reference (blue dots).

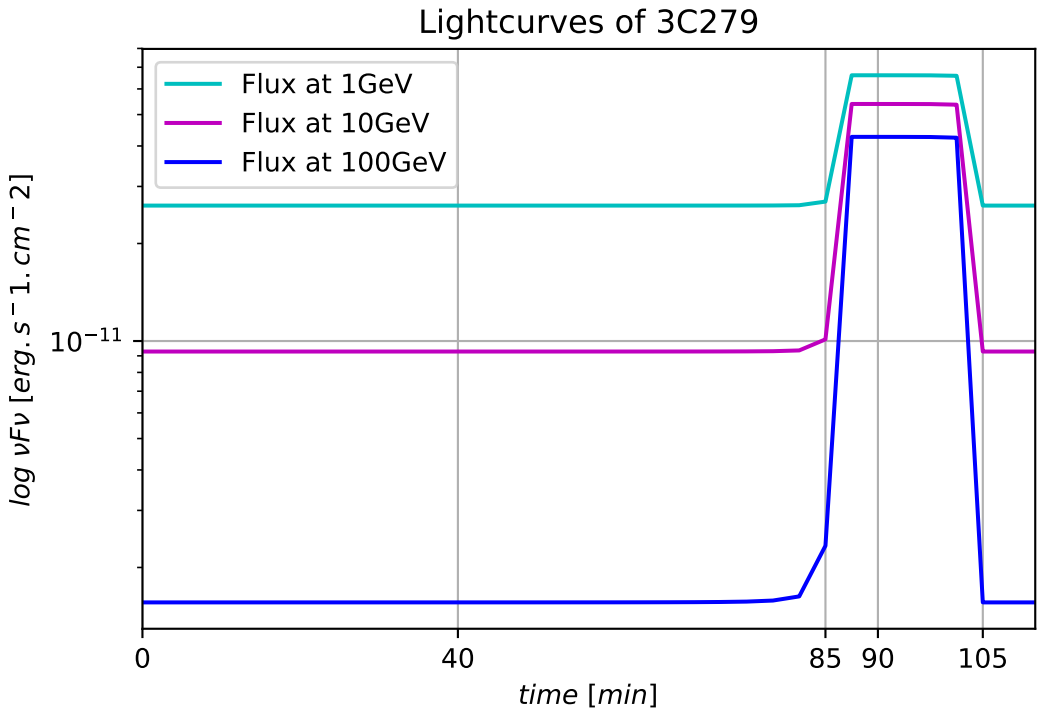

Figure 6.4: The lightcurve of 3C279 for the energies of 1 GeV, 10 GeV and 100 GeV.

Chapter 7

Summary and Conclusions

In this dissertation the hadronic synchrotron mirror model is used to explain the orphan TeV flare of 3C 279 that was observed on 28 of January 2018. Eleven days after a Fermi-LAT flare was observed with counterparts in the X-ray and optical bands, an orphan flare in the VHE γ-ray band was detected. The feasibility of the synchrotron mirror model was estimated using a semi-analytical approach where the target photon density for photo-pion production is calculated from basic principles. We compared this to the photon density found by equating the photo-pion energy loss rate with that of the synchrotron energy loss rate. The required target photon energy density to produce a pion-decay signature comparable to the proton-synchrotron flux was calculated as 280 erg$\cdot$cm^{-3}, while the estimated actual target photon energy density for standard parameters was 35.2 erg$\cdot$cm^{-3} with an order of magnitude difference. Conclusively, the target photon field was dense enough for photo-pion production to take place sufficiently for its emission to be comparable to that of the Fermi-LAT flux if some of the parameters are adjusted. The numerically evaluated target photon density was larger than estimated from the analytical approach. To get a good representation of the flare spectrum I deviated from the standard parameters. The radius of the cloud was changed from $R_{cl} = 10^{17}$ cm, a more standard cloud size, to $R_{cl} = 5 \times 10^{15}$ cm. With a smaller cloud the reflective fraction also had to be smaller, we changed it from $\tau = 0.1$ to $\tau = 0.001$. The other parameters were adjusted as listed at the start of Chapter 6, to fit the proton synchrotron spectrum.

The Fermi-LAT spectrum was fitted with a proton-synchrotron emission component, which allowed us to fix the parameters of the relativistic proton population in the emission region. The hadronic synchrotron mirror model postulates that the orphan TeV flare is produced by photo-pion production cascades. A numerical code was developed to evaluate the hadronic synchrotron mirror model and explore the free parameter space to look for plausible solutions that would produce the observed orphan flare.

The synchrotron mirror scenario induces a dense enough target photon field

to produce the observed orphan flare. This model does predict a moderate flare in Fermi-LAT, but with a much smaller amplitude than that of the VHE flare. This suggests that protons are accelerated to ultra-relativistic energies. For these protons to be accelerated to these very-high energies, a strong magnetic environment is needed; in our study, $B = 100\ G$ was used as the magnetic field strength. Highly magnetised plasma may lead to rapid variability. The lightcurves displayed expected behaviour with a sudden rise in flux in the H.E.S.S. observational range and only had a slight increase in the Fermi-LAT range. The flare duration is predicted to be about half an hour long, which is the run time of one H.E.S.S. observational run. Fermi-LAT typically needs longer integration times than half an hour to get a significant detection of 3C279, which could explain why no flare was seen in the Fermi-LAT light curve.

The natural next step would be to search for neutrino signatures and emission. A comparative study of different models and the SEDs and lightcurves they produce will lead to more conclusive results regarding the variability and jet composition, as well as neutrino emission connected to these orphan flare events. This will be done in my PhD in Astrophysics; the model will be compared to other viable models: Multi-zone, combined lepto-hadronic and Spine-sheath models. Detection of neutrino emission will also test the models.

Bibliography

Alexander Aab, Pedro Abreu, Marco Aglietta, Justin M Albury, Ingomar Allekotte, Alejandro Almela, Jaime Alvarez-Muñiz, R Alves Batista, Gioacchino Alex Anastasi, Luis Anchordoqui, et al. A search for ultra-high-energy neutrinos from txs 0506+ 056 using the pierre auger observatory. *The Astrophysical Journal*, 902(2):105, 2020.

F Aharonian, AG Akhperjanian, AR Bazer-Bachi, B Behera, M Beilicke, W Benbow, D Berge, K Bernlöhr, C Boisson, O Bolz, et al. An exceptional very high energy gamma-ray flare of pks 2155–304. *The Astrophysical Journal Letters*, 664(2):L71, 2007.

FA Aharonian. Tev gamma rays from bl lac objects due to synchrotron radiation of extremely high energy protons. *New Astronomy*, 5(7):377–395, 2000.

Jord Albert, E Aliu, H Anderhub, LA Antonelli, P Antoranz, M Backes, C Baixeras, JA Barrio, H Bartko, D Bastieri, et al. Very-high-energy gamma rays from a distant quasar: how transparent is the universe? *Science*, 320(5884): 1752–1754, 2008.

Maxim V Barkov, Felix A Aharonian, Sergey V Bogovalov, Stanislav R Kelner, and Dmitry Khangulyan. Rapid tev variability in blazars as a result of jet-star interaction. *The Astrophysical Journal*, 749(2):119, 2012.

Mitchell C Begelman, Andrew C Fabian, and Martin J Rees. Implications of very rapid tev variability in blazars. *Monthly Notices of the Royal Astronomical Society: Letters*, 384(1):L19–L23, 2008.

Stefano Bianchi, Roberto Maiolino, and Guido Risaliti. Agn obscuration and the unified model. *Advances in Astronomy*, 2012, 2012.

Roger Blandford, David Meier, and Anthony Readhead. Relativistic jets from active galactic nuclei. *Annual Review of Astronomy and Astrophysics*, 57: 467–509, 2019.

D Blinov, V Pavlidou, I Papadakis, S Kiehlmann, I Liodakis, GV Panopoulou, E Angelakis, M Baloković, T Hovatta, OG King, et al. Robopol: Connection between optical polarization plane rotations and gamma-ray flares in blazars. *Monthly Notices of the Royal Astronomical Society*, 474(1):1296–1306, 2018.

Steven D Bloom and Alan P Marscher. An analysis of the synchrotron self-compton model for the multi–wave band spectra of blazars. *The Astrophysical Journal*, 461:657, 1996.

M Böttcher. A hadronic synchrotron mirror model for the "orphan" TeV flare in 1es 1959+ 650. *The Astrophysical Journal*, 621(1):176, 2005.

M Böttcher. Modeling the emission processes in blazars. In *The Multi-Messenger Approach to High-Energy Gamma-Ray Sources*, pages 95–104. Springer, 2007.

M Böttcher, A Reimer, K Sweeney, and A Prakash. Leptonic and hadronic modeling of fermi-detected blazars. *The Astrophysical Journal*, 768(1):54, 2013.

Markus Böttcher. Progress in multi-wavelength and multi-messenger observations of blazars and theoretical challenges. *Galaxies*, 7(1):20, 2019.

Markus Böttcher and Charles D Dermer. High-energy gamma rays from ultra-high-energy cosmic-ray protons in gamma-ray bursts. *The Astrophysical Journal Letters*, 499(2):L131, 1998.

Markus Böttcher, Daniel E Harris, and Henric Krawczynski. *Relativistic Jets from Active Galactic Nuclei*, volume 1. Wiley Online Library, 2012.

Arnon Dar and Ari Laor. Hadronic production of tev gamma-ray flares from blazars. *The Astrophysical Journal Letters*, 478(1):L5, 1997.

Mathieu de Naurois and Daniel Mazin. Ground-based detectors in very-high-energy gamma-ray astronomy. *Comptes Rendus Physique*, 16(6-7):610–627, 2015.

Charles D Dermer and Reinhard Schlickeiser. Model for the high-energy emission from blazars. *The Astrophysical Journal*, 416:458, 1993.

Anton Dmytriiev. *Exploring Active Galactic Nuclei at extreme energies: analysis and modeling of multi-wavelength flares and preparation of CTA*. PhD thesis, November 2020.

Fermi-LAT. A change in the optical polarization associated with a γ-ray flare in the blazar 3c 279. *Nature*, 463(7283):919, 2010.

G al Fossati, L Maraschi, A Celotti, A Comastri, and G Ghisellini. A unifying view of the spectral energy distributions of blazars. *Monthly Notices of the Royal Astronomical Society*, 299(2):433–448, 1998.

C Martin Gaskell. What broad emission lines tell us about how active galactic nuclei work. *New Astronomy Reviews*, 53(7-10):140–148, 2009.

G Ghisellini, A Celotti, G Fossati, L Maraschi, and A Comastri. A theoretical unifying scheme for gamma-ray bright blazars. *Monthly Notices of the Royal Astronomical Society*, 301(2):451–468, 1998.

Gabriele Ghisellini. The blazar sequence 2.0. *Galaxies*, 4(4):36, 2016.

Berrie Giebels and H.E.S.S. Collaboration. Status and recent results from hess. *arXiv preprint arXiv:1303.2850*, 2013.

Minfeng Gu, Xinwu Cao, and DR Jiang. On the masses of black holes in radio-loud quasars. *Monthly Notices of the Royal Astronomical Society*, 327(4): 1111–1115, 2001.

RC Hartman, DL Bertsch, CE Fichtel, SD Hunter, G Kanbach, DA Kniffen, PW Kwok, YC Lin, JR Mattox, HA Mayer-Hasselwander, et al. Detection of high-energy gamma radiation from quasar 3c 279 by the egret telescope on the compton gamma ray observatory. *The Astrophysical Journal*, 385:L1–L4, 1992.

RC Hartman, M Böttcher, G Aldering, H Aller, M Aller, DE Backman, TJ Balonek, DL Bertsch, SD Bloom, H Bock, et al. Multiepoch multiwavelength spectra and models for blazar 3c 279. *The Astrophysical Journal*, 553 (2):683, 2001.

M Hayashida, GM Madejski, K Nalewajko, M Sikora, AE Wehrle, P Ogle, W Collmar, Stefan Larsson, Y Fukazawa, R Itoh, et al. The structure and emission model of the relativistic jet in the quasar 3c 279 inferred from radio to high-energy γ-ray observations in 2008-2010. *The Astrophysical Journal*, 754(2):114, 2012.

M Hayashida, K Nalewajko, GM Madejski, M Sikora, R Itoh, M Ajello, RD Blandford, S Buson, J Chiang, Yasushi Fukazawa, et al. Rapid variability of blazar 3c 279 during flaring states in 2013- 2014 with joint fermi-lat, nustar, swift, and ground-based multi-wavelength observations. *The Astrophysical Journal*, 807(1):79, 2015.

W Jaffe, K Meisenheimer, HJA Röttgering, Ch Leinert, A Richichi, O Chesneau, D Fraix-Burnet, A Glazenborg-Kluttig, G-L Granato, U Graser, et al. The central dusty torus in the active nucleus of ngc 1068. *Nature*, 429(6987):47–49, 2004.

JM Jauch and F Rohrlich. Theory of the external field. In *The Theory of Photons and Electrons*, pages 302–326. Springer, 1976.

KENNETH J Johnston, ALAN L Fey, NORBERT Zacharias, JANE L Russell, CHOPO Ma, CHRISTIAN de Vegt, JOHN E Reynolds, DAVID L Jauncey, BRENT A Archinal, MS Carter, et al. A radio reference frame. *The Astronomical Journal*, 110:880, 1995.

Svetlana G Jorstad, Alan P Marscher, Matthew L Lister, Alastair M Stirling, Timothy V Cawthorne, José-Luis Gómez, and Walter K Gear. Change in speed and direction of the jet near the core in the quasar 3c 279. *The Astronomical Journal*, 127(6):3115, 2004.

B Kapanadze, Patrizia Romano, STEFANO Vercellone, and S Kapanadze. The x-ray behaviour of the high-energy peaked bl lacertae source pks 2155- 304 in the 0.3–10 kev band. *Monthly Notices of the Royal Astronomical Society*, 444(2):1077–1094, 2014.

Jae-Young Kim, Thomas P Krichbaum, Avery E Broderick, Maciek Wielgus, Lindy Blackburn, José L Gómez, Michael D Johnson, Katherine L Bouman, Andrew Chael, Kazunori Akiyama, et al. Event horizon telescope imaging of the archetypal blazar 3c 279 at an extreme 20 microarcsecond resolution. *Astronomy & Astrophysics*, 640:A69, 2020.

Motoki Kino, Fumio Takahara, and Masaaki Kusunose. Energetics of tev blazars and physical constraints on their emission regions. *The Astrophysical Journal*, 564(1):97, 2002.

A Konopelko, Apostolos Mastichiadis, J Kirk, Ocker C de Jager, and Floyd W Stecker. Modeling the tev gamma-ray spectra of two low-redshift active galactic nuclei: Markarian 501 and markarian 421. *The Astrophysical Journal*, 597 (2):851, 2003.

H Krawczynski, SB Hughes, D Horan, F Aharonian, MF Aller, H Aller, P Boltwood, J Buckley, P Coppi, G Fossati, et al. Multiwavelength observations of strong flares from the TeV blazar 1es 1959+ 650. *The Astrophysical Journal*, 601(1):151, 2004.

M Kusunose and F Takahara. A structured leptonic jet model of the "orphan" TeV gamma-ray flares in TeV blazars. *The Astrophysical Journal*, 651(1):113, 2006.

VM Larionov, SG Jorstad, AP Marscher, CM Raiteri, M Villata, I Agudo, MF Aller, AA Arkharov, IM Asfandiyarov, U Bach, et al. Results of webt, vlba and rxte monitoring of 3c 279 during 2006–2007. *Astronomy & Astrophysics*, 492(2):389–400, 2008.

Matthiew L Lister, MF Aller, HD Aller, Daniel C Homan, KI Kellermann, Yuri Y Kovalev, AB Pushkarev, JL Richards, E Ros, and Tuomas Savolainen. Mojave. x. parsec-scale jet orientation variations and superluminal motion in active galactic nuclei. *The Astronomical Journal*, 146(5):120, 2013.

Malcolm S Longair. *High energy astrophysics*. Cambridge university press, 2011.

CR Lynds, AN Stockton, and WC Livingston. New spectroscope observations of quasi-stellar sources. *The Astrophysical Journal*, 142:1667, 1965.

Nicholas R MacDonald, Svetlana G Jorstad, and Alan P Marscher. "orphan" γ-ray flares and stationary sheaths of blazar jets. *The Astrophysical Journal*, 850(1):87, 2017.

K Mannheim and PL Biermann. Gamma-ray flaring of 3c 279-a proton-initiated cascade in the jet? *Astronomy and Astrophysics*, 253:L21–L24, 1992.

Karl Mannheim. The proton blazar. *Astronomy and Astrophysics*, 269:67–76, 1993.

L Maraschi, G Ghisellini, and A Celotti. A jet model for the gamma-ray emitting blazar 3c 279. *The Astrophysical Journal*, 397:L5–L9, 1992.

L Maraschi, P Grandi, CM Urry, AE Wehrle, GM Madejski, HH Fink, G Ghisellini, RC Hartman, AP Koratkar, C Von Montigny, et al. The 1993 multiwavelength campaign on 3c 279: The radio to gamma-ray energy distribution inlow state. *The Astrophysical Journal*, 435:L91–L95, 1994.

Alan P Marscher. Turbulent, extreme multi-zone model for simulating flux and polarization variability in blazars. *The Astrophysical Journal*, 780(1):87, 2013.

P Marziani, JW Sulentic, D Dultzin-Hacyan, M Calvani, and M Moles. Comparative analysis of the high-and low-ionization lines in the broad-line region of active galactic nuclei. *The Astrophysical Journal Supplement Series*, 104: 37, 1996.

A Mücke, Ralph Engel, JP Rachen, RJ Protheroe, and Todor Stanev. Monte carlo simulations of photohadronic processes in astrophysics. *Computer Physics Communications*, 124(2-3):290–314, 2000.

A Mücke, RJ Protheroe, R Engel, JP Rachen, and T Stanev. Bl lac objects in the synchrotron proton blazar model. *Astroparticle Physics*, 18(6):593–613, 2003.

Paolo Padovani. The blazar sequence: validity and predictions. *Astrophysics and Space Science*, 309(1-4):63–71, 2007.

Vaidehi S Paliya, S Sahayanathan, and CS Stalin. Multi-wavelength observations of 3c 279 during the extremely bright gamma-ray flare in 2014 march–april. *The Astrophysical Journal*, 803(1):15, 2015.

SR Patel, D Bose, Nayantara Gupta, and M Zuberi. Broadband modelling of orphan gamma ray flares. *Journal of High Energy Astrophysics*, 29:31–39, 2021.

Maria Petropoulou, Kohta Murase, Derek Brindley Fox, and Nobuyuki Kawai. Neutrinos from hadronic cascades: the case of the 2014-15 neutrino flare from txs 0506+ 056. *HEAD*, pages 106–35, 2019.

Elena Pian, Eliana Palazzi, Lucio Chiappetti, Laura Maraschi, Fabrizio Tavecchio, Gabriele Ghisellini, Gianpiero Tagliaferri, Giovanni Fossati, Aldo Treves, Claudia Megan Urry, et al. Bepposax observations of the bl lac object mkn 501 in an intermediate state. *arXiv preprint astro-ph/9810398*, 1998.

William J Potter. Modelling blazar flaring using a time-dependent fluid jet emission model–an explanation for orphan flares and radio lags. *Monthly Notices of the Royal Astronomical Society*, 473(3):4107–4121, 2018.

Anita Reimer, Markus Böttcher, and Sara Buson. Cascading constraints from neutrino-emitting blazars: the case of txs 0506+ 056. *The Astrophysical Journal*, 881(1):46, 2019.

Gustavo E Romero, Markus Boettcher, Sera Markoff, and Fabrizio Tavecchio. Relativistic jets in active galactic nuclei and microquasars. *Space Science Reviews*, 207(1-4):5–61, 2017.

George B Rybicki and Alan P Lightman. *Radiative processes in astrophysics*. John Wiley & Sons, 2008.

RM Sambruna, FA Aharonian, H Krawczynski, AG Akhperjanian, JA Barrio, K Bernlöhr, H Bojahr, I Calle, JL Contreras, J Cortina, et al. Correlated intense x-ray and tev activity of markarian 501 in 1998 june. *The Astrophysical Journal*, 538(1):127, 2000.

Allan Sandage and John D Wyndham. On the optical identification of eleven new quasi-stellar radio sources. *The Astrophysical Journal*, 141:328, 1965.

Marek Sikora and Greg Madejski. On pair content and variability of subparsec jets in quasars. *The Astrophysical Journal*, 534(1):109, 2000.

C Megan Urry and Paolo Padovani. Unified schemes for radio-loud active galactic nuclei. *Publications of the Astronomical Society of the Pacific*, 107(715): 803, 1995.

AE Wehrle, E Pian, CM Urry, L Maraschi, IM McHardy, AJ Lawson, G Ghisellini, RC Hartman, GM Madejski, F Makino, et al. Multiwavelength observations of a dramatic high-energy flare in the blazar 3c 279. *The Astrophysical Journal*, 497(1):178, 1998a.

Ann E Wehrle, E Pian, CM Urry, L Maraschi, IM McHardy, AJ Lawson, G Ghisellini, RC Hartman, GM Madejski, F Makino, et al. Multiwavelength observations of a dramatic high-energy flare in the blazar 3c 279. *The Astrophysical Journal*, 497(1):178, 1998b.

Jong-Hak Woo and C Megan Urry. Active galactic nucleus black hole masses and bolometric luminosities. *The Astrophysical Journal*, 579(2):530, 2002.

JA Zensus and RW Porcas. Search for superluminal motion in the weak cores of extended quasars. In *Symposium-International astronomical union*, volume 119, pages 167–168. Cambridge University Press, 1986.

Haocheng Zhang and Markus Boettcher. X-ray and gamma-ray polarization in leptonic and hadronic jet models of blazars. *The Astrophysical Journal*, 774 (1):18, 2013.